Chapter 2
Mathematical Representation of Scattered Fields from Chipless RFID Tags

2.1 Introduction

As previously mentioned, a chipless RFID system is comprised of three basic components: reader, antenna, and chipless tag. The antenna illuminates the reader area and induces currents on the metallic tags. The induced currents re-radiate the scattered fields, which will be processed in the reader for decoding the IDs of the tags. The scattering phenomena is a sophisticated process, which can be described in a simple mathematical model. This mathematical model provides us insight of the electromagnetic behavior of the structure, which is useful in the design process of chipless RFID tags. The induced currents on the tag structure can be expanded in different ways. One method is to expand the induced currents versus the singularity poles of the tag, which is the basis of the singularity expansion method (SEM). In such a representation, the solution is expressed as a collection of poles, branch cuts, and an entire function in the complex frequency plane. In this chapter, after a comprehensive study of the SEM, the wavefront representation of the SEM is presented to describe the scattering mechanisms in the early-time and late-time modes. Altes' model is employed to describe the early-time response using the impulse responses of the scattering centers of the scatterer. Subsequently, the equivalent circuit of the scatterer is introduced based on the SEM representation of the fields. As an example, the current modes and associated radiated fields from a dipole antenna are studied.

On the other hand, the induced currents can be expanded versus the eigenmodes of the scatterer, which are found from an eigenvalue equation governing the structure under consideration. The singularity poles of the structure are related to the zeroes of the eigenvalues of the impedance matrix in the complex frequency plane. This relationship is computationally easy in extracting the complex natural resonances (CNRs) of the well-coordinated structures from the eigenmode expansion of the fields. As a simple case, the fields in a rectangular cavity resonator are represented versus the eigenmodes of its equivalent eigenvalue equation and the

R. Rezaiesarlak, M. Manteghi, *Chipless RFID*, DOI 10.1007/978-3-319-10169-9_2

relationship between the eigenvalues and singularity poles of the cavity is clearly shown in a closed-form representation.

As a weighted eigenvalue decomposition, the theory of characteristic modes is presented and effectively employed for analyzing the scattered fields from the chipless RFID tags. In this method, the current on the scatterer is mapped into a new set of characteristic modes, which are in-phase on the surface of the scatterer. Then, the currents are expanded versus these real-value characteristic modes. The characteristic-mode theory simplifies analysis of the induced currents, their related fields, and their behavior at different frequencies.

2.2 Singularity Expansion Method (SEM)

The concept of the singularity expansion method (SEM) was first introduced in 1971 by Carl Baum after observing the time-domain backscattered signal from missiles. By illuminating the target with a wideband pulse, it was observed that the time-domain returned signal from the missile includes some fast variations followed by damped sinusoidal signals. The history of SEM begins with a meeting at Northrop Corporate Laboratories in Pasadena, CA, in September 1971 [1]. After that meeting, Baum formulated the SEM in the Interaction note 88 [2]. He applied the proposed method to a perfectly conducting sphere and obtained the poles of the sphere in layers in the complex s-plane. After the advent of SEM, the proposed technique was broadly employed for the transient analysis of scatterers and antennas [2–10]. In [11–14], SEM was used to characterize the time and frequency-domain features of antennas and channels. Additionally, many researchers in the radar discipline employed SEM in identifying targets in military applications [15–18] and ground penetration radars [19–21]. Later on, the proposed technique was used in identifying and designing chipless RFID tags [22–24], breast cancer detection [25, 26], and monitoring the deployment of arterial stents implanted in blood vessels [27].

2.2.1 Singularity Expansion Method in Circuit Theory

The concept of the singularity expansion method (SEM) has been widely used in circuit theory for a long time [28]. As a simple case, an RLC-series resonator in Fig. 2.1a is considered, which is connected to a voltage source $v(t)$. The input impedance of a high-Q electrically small antenna can be modeled by this simple RLC circuit for a narrow frequency range [29–31]. The differential equation concerning the current in the circuit is

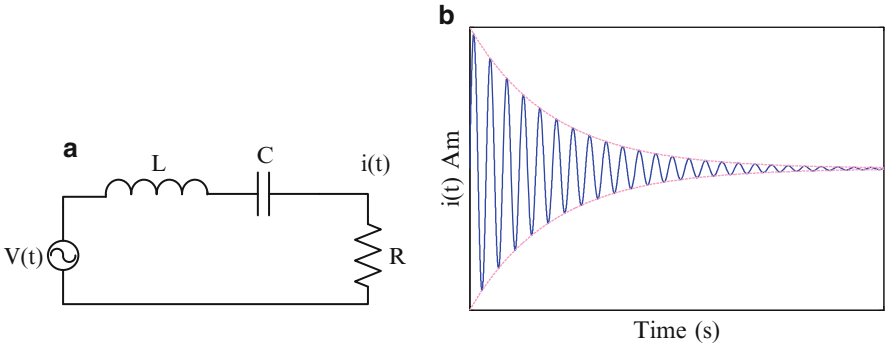

Fig. 2.1 (**a**) Series RLC circuit. (**b**) Impulse response of the circuit in time domain

$$\left(L\frac{d^2}{dt^2}+R\frac{d}{dt}+\frac{1}{C}\right)i(t)=\frac{dv(t)}{dt} \tag{2.1}$$

By applying the Laplace transform to (2.1) and assuming zero initial conditions for the voltage across the capacitor and current through the inductor, the current is written by

$$\begin{aligned} I(s) &= \frac{Cs}{\left(\frac{s}{\omega_0}\right)^2+\frac{1}{Q}\left(\frac{s}{\omega_0}\right)+1}\cdot V(s) \\ &= Y(s)\cdot V(s) \end{aligned} \tag{2.2}$$

Here, the radian resonant frequency, ω_0, and the quality factor at the resonant frequency, Q, are defined as

$$\omega_0=\frac{1}{\sqrt{LC}} \tag{2.3}$$

$$Q=\frac{1}{\omega_0 RC} \tag{2.4}$$

The admittance function, Y(s), can be expanded versus first-order poles of the circuit as

$$Y(s)=\frac{D}{s-s_1}+\frac{D^*}{s-s_1{}^*} \tag{2.5}$$

where $s_1=\alpha_1+j\omega_1$ is the complex natural resonance (CNR) of the circuit. The damping factor, resonant frequency, and D in (2.5) are given by

$$\alpha_1 = \frac{-\omega_0}{2Q} \tag{2.6}$$

$$\omega_1 = \frac{\omega_0}{2}\sqrt{4 - \frac{1}{Q^2}} \tag{2.7}$$

$$D = \frac{C}{2}\left(1 + j\frac{1+\alpha_1}{\omega_1}\right) \tag{2.8}$$

For $Q \geq 0.5$, the circuit resonates at $f_1 = \omega_1/(2\pi)$. The residue of the pole in (2.2) is equal to $DV(s)$. Although the pole of the circuit is independent of the input voltage, the residue will change with variations in the input voltage. The impulse response of the circuit in the time domain is obtained as (2.9) by assuming $V(s) = 1$ in (2.2) and applying the inverse Laplace transform.

$$i(t) = |D|e^{-\alpha_1 t}\cos\left(\omega_1 t + \angle D\right) \tag{2.9}$$

Here, $i(t)$ is a damped sinusoidal current in the time domain as shown in Fig. 2.1b. Therefore, each complex natural resonance of a circuit acts as a damped sinusoidal signal in the time domain whose amplitude is related to the applied source. The above discussion can be easily generalized to multi-resonant circuits.

In a multi-resonant circuit, the input admittance of the circuit is expanded versus the singularity poles of the circuit as

$$Y(s) = F(s) + \sum_{n=-N}^{N} \frac{D_n}{s - s_n} \tag{2.10}$$

where N is the number of the CNRs, s_n, of the circuit and $F(s)$ is the entire function including the non-resonant part of the circuit [32]. In distributed circuits, such as cavity and transmission-line resonators where the number of resonances is infinity ($N \to \infty$), the entire function accelerates the convergence of the series [32].

2.2.2 *Singularity Expansion Method in Transient Scattering*

In order to study the scattering mechanism in chipless RFID systems, a 3-bit chipless RFID tag shown in Fig. 2.2 is illuminated by an incident field ($\mathbf{E}^{\mathbf{inc}}$, $\mathbf{H}^{\mathbf{inc}}$), launched from a transmitting antenna. The surrounding medium is assumed to be free space with permittivity ε_0 and permeability μ_0. The ID of the tag is set in the resonant frequencies of the structure, which can be embedded into some resonant-based circuitry on the tag. In practical applications, it is beneficial to design the tag on a metallic surface in order to maximize the radiation efficiency of the scatterer. Assuming the induced current on the tag as $\mathbf{J}$, the scattered field is obtained from either an electric-field integral equation (EFIE) or a magnetic-field

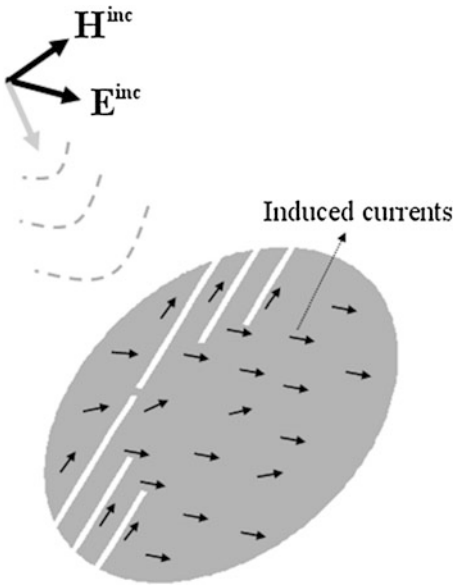

Fig. 2.2 3-bit tag illuminated by an incident plane wave

integral equation (MFIE) [33]. Here, the former case is considered for simplicity in formulations. Therefore, the scattered electric field is written in the Laplace domain as [34]

$$\mathbf{E}^{\mathbf{s}}(\mathbf{r};s) = -\mu s \iint_A \left[\left(\overleftrightarrow{\mathbf{I}} - \frac{1}{k^2} \nabla \nabla \right) G_0\left(\mathbf{r}, \mathbf{r}^{'}; s\right) \right] \cdot \mathbf{J}\left(\mathbf{r}^{'}; s\right) dS^{'} \tag{2.11}$$

where $\overleftrightarrow{\mathbf{I}} = \hat{x}\hat{x} + \hat{y}\hat{y} + \hat{z}\hat{z}$, $s = \alpha + \mathrm{j}\omega$ is the complex frequency, $k = s/c$ represents the propagation constant of the fields in the complex frequency domain, and A is the surface of the tag. The primed and unprimed coordinates represent the source and observation points, respectively. The quantity G_0 is the scalar Green's function in free space.

$$G_0\left(\mathbf{r}, \mathbf{r}^{'}; s\right) = \frac{e^{-jk|\mathbf{r}-\mathbf{r}^{'}|}}{4\pi|\mathbf{r}-\mathbf{r}^{'}|} \tag{2.12}$$

G_0 satisfies the Sommerfeld radiation condition as

$$\lim_{r\to\infty} r\left(\frac{\partial}{\partial r} + jk\right) G_0\left(\mathbf{r}, \mathbf{r}^{'}; s\right) = 0 \tag{2.13}$$

The scattered field in (2.11) can be written as the inner product of the dyadic Green's function and current distribution on the structure as

$$\mathbf{E}^{s}(\mathbf{r};s) = \left\langle \overleftrightarrow{\mathbf{G}}\left(\mathbf{r},\mathbf{r}';s\right), \mathbf{J}\left(\mathbf{r}';s\right) \right\rangle_{r'} \tag{2.14}$$

where the dyadic Green's function is defined as

$$\overleftrightarrow{\mathbf{G}}\left(\mathbf{r},\mathbf{r}';s\right) = -\mu s\left(\overleftrightarrow{\mathbf{I}} - \frac{1}{k^2}\nabla\nabla\right) G_0\left(\mathbf{r},\mathbf{r}';s\right) \tag{2.15}$$

The associated radiation condition for $\overleftrightarrow{\mathbf{G}}$ is

$$\lim_{r\to\infty} r(\nabla \times + jk\hat{r} \times)\overleftrightarrow{\mathbf{G}}\left(\mathbf{r},\mathbf{r}';s\right) = \mathbf{0} \tag{2.16}$$

and inner product in (2.14) is defined by

$$\langle \mathbf{A},\mathbf{B}\rangle_a = \int \mathbf{A}\cdot\mathbf{B}\ da \tag{2.17}$$

Assuming the tag is a perfect electric conductor (PEC), the boundary condition on the tag surface is given by

$$\hat{t}\,.\left(\mathbf{E}^{s}(\mathbf{r};s) + \mathbf{E}^{\text{inc}}(\mathbf{r};s)\right) = \mathbf{0} \qquad \forall \mathbf{r} \in A \tag{2.18}$$

where $\hat{t}$ denotes the unit vector tangential to the tag surface. As a result, the electric-field integral equation (EFIE) is written by

$$\left\langle \overleftrightarrow{\mathbf{G}}\left(\mathbf{r},\mathbf{r}'\right), \mathbf{J}\left(\mathbf{r}'\right) \right\rangle_{\mathbf{r}'} = -\mathbf{E}_{\text{t}}^{\text{inc}}(\mathbf{r}) \qquad \forall \mathbf{r} \in A \tag{2.19}$$

Subscript t in (2.19) indicates the tangential components of the fields on the tag surface. The method of moment (MoM) can be used to solve equation (2.19). By discretizing the surface of the tag into N isolated meshes and applying Galerkin's technique, one can write

$$\Gamma_{\text{mn}} \cdot \text{J}_{\text{n}} = \text{I}_{\text{n}} \tag{2.20}$$

The matrix equation in (2.20) should be in some sense an accurate representation of the integral equation in (2.19). One important criterion of such accuracy is the convergence of the solution obtained from (2.19) to the real current distribution as $N \to \infty$ [33]. The current distribution on the tag is obtained from

$$\text{J}_{\text{n}} = {\Gamma_{\text{mn}}}^{-1} \cdot \text{I}_{\text{n}} \tag{2.21}$$

According to (2.21), the singularity poles of the tag are the zeroes of the determinant of the coefficient matrix Γ as

$$\det(\Gamma(s_k)) = 0 \qquad k = 1,\ 2,\ 3\ldots \tag{2.22}$$

These singularity poles are the CNRs of the tag at which the current distribution on the tag shows damped oscillating behavior after the incident source field crosses through the tag. The basis of the SEM is that the current distribution is assumed to be an analytic function in the complex s-plane, except at CNRs such as

$$\mathbf{J}(\mathbf{r}; s) = \sum_{n=-\infty}^{+\infty} \frac{\mathbf{a}_n(\mathbf{r}; s)}{s - s_n} + \mathbf{J}_e(\mathbf{r}; s) \tag{2.23}$$

where $s_n = \alpha_n + j\omega_n$ is the nth CNR of the tag. Since the time-domain response is a real-valued signal, then

$$\begin{aligned} s_n &= s_{-n}{}^* \\ \mathbf{a}_n(\mathbf{r}; s^*) &= [\mathbf{a}_n(\mathbf{r}; s)]^* \\ \mathbf{J}_e(\mathbf{r}; s^*) &= [\mathbf{J}_e(\mathbf{r}; s)]^* \end{aligned} \tag{2.24}$$

Equation (2.23) needs some more interpretation. According to Mittag-Leffler's theorem, an entire function in the s-plane is required for each pole in the infinite series to guarantee the convergence of the series [33, 35]. This entire function is represented by $\mathbf{J_e}(\mathbf{r};\ s)$ in (2.23). The other important part of the series is the weighting function $\mathbf{a}_n(\mathbf{r}; s)$, which is assumed separable in the spectral-spatial form of

$$\mathbf{a}_n(\mathbf{r}; s) = R_n(s)\mathbf{J}_n(\mathbf{r}) \tag{2.25}$$

Here, $\mathbf{J}_n(\mathbf{r})$ is the natural mode of the tag at the nth resonant frequency, and $R_n(s)$ is the corresponding frequency-dependent residue of the pole. By inserting (2.25) in (2.23), the current distribution close to s_n is written by

$$\mathbf{J}(\mathbf{r}; s) = \frac{R_n(s)\mathbf{J}_n(\mathbf{r})}{s - s_n} + \mathbf{J}_e(\mathbf{r}; s) \tag{2.26}$$

By expanding $\overleftrightarrow{\mathbf{G}}$ and the incident source field, $\mathbf{E}^{\text{inc}}$, in a power series around $s = s_n$ as

$$\overleftrightarrow{\mathbf{G}}\left(\mathbf{r}, \mathbf{r}'; s\right) = \sum_{m=0}^{\infty} \frac{1}{m!} \frac{\partial^m \overleftrightarrow{\mathbf{G}}\left(\mathbf{r}, \mathbf{r}'; s\right)}{\partial s^m}\bigg|_{s=s_n} (s - s_n)^m \tag{2.27}$$

$$\mathbf{E}_{\mathrm{t}}^{\mathrm{inc}}(\mathbf{r};s)=\sum_{m=0}^{\infty}\frac{1}{m!}\left.\frac{\partial^m\mathbf{E}_{\mathrm{t}}^{\mathrm{inc}}(\mathbf{r};s)}{\partial s^m}\right|_{s=s_{\mathrm{n}}}(s-s_{\mathrm{n}})^m \tag{2.28}$$

and inserting (2.27) and (2.28) in (2.19), one can write

$$\begin{aligned}&\left\langle\overleftrightarrow{\mathbf{G}}\left(\mathbf{r},\mathbf{r}';s_{\mathrm{n}}\right)+(s-s_{\mathrm{n}})\left.\frac{\partial\overleftrightarrow{\mathbf{G}}\left(\mathbf{r},\mathbf{r}';s\right)}{\partial s}\right|_{s=s_{\mathrm{n}}}+\cdots,\frac{R_{\mathrm{n}}(s_{\mathrm{n}})\mathbf{J}_{\mathrm{n}}\left(\mathbf{r}'\right)}{s-s_{\mathrm{n}}}+\mathbf{J}_e\left(\mathbf{r}';s\right)\right\rangle_{\mathbf{r}'}\\&=-\mathbf{E}_{\mathrm{t}}^{\mathrm{inc}}(\mathbf{r};s_{\mathrm{n}})-(s-s_{\mathrm{n}})\left.\frac{\partial\mathbf{E}_{\mathrm{t}}^{\mathrm{inc}}(\mathbf{r};s)}{\partial s}\right|_{s=s_{\mathrm{n}}}-\cdots\end{aligned} \tag{2.29}$$

By balancing the two sides of (2.29) according to powers of $(s-s_n)$, some important expressions are obtained. The coefficient of the $(s-s_{\mathrm{n}})^{-1}$ term at $s=s_{\mathrm{n}}$ gives

$$\left\langle\overleftrightarrow{\mathbf{G}}\left(\mathbf{r},\mathbf{r}';s_{\mathrm{n}}\right),\mathbf{J}_{\mathrm{n}}\left(\mathbf{r}'\right)\right\rangle_{\mathbf{r}'}=\mathbf{0} \tag{2.30}$$

Equation (2.30) provides some important features of the CNRs and corresponding natural modes. By converting (2.30) to matrix form, it is seen that the determinant of the coefficient matrix should be zero at CNRs in order to have nontrivial solutions. As another significant point, these poles are completely dependent upon the dyadic Green's function of the structure and as (2.30) illustrates, they are source-free and aspect-independent parameters of the tag. This is the reason that these parameters are often used in identification applications. For each CNR, s_n, there is a nontrivial natural mode, $\mathbf{J}_{\boldsymbol{n}}(\mathbf{r})$, which is the solution of (2.30). Corresponding to (2.30), one can define the coupling factors as the solutions to the following homogenous equation

$$\left\langle\mathbf{M}_{\mathrm{n}}\left(\mathbf{r}'\right),\overleftrightarrow{\mathbf{G}}\left(\mathbf{r},\mathbf{r}';s_{\mathrm{n}}\right)\right\rangle_{\mathbf{r}'}=\mathbf{0} \tag{2.31}$$

By equating the coefficients of $(s-s_{\mathrm{n}})^0$ in both sides of (2.29), one has

$$\begin{aligned}&\left\langle\overleftrightarrow{\mathbf{G}}\left(\mathbf{r},\mathbf{r}';s_{\mathrm{n}}\right),\mathbf{J}_e\left(\mathbf{r}';s\right)\right\rangle_{\mathbf{r}'}+R_{\mathrm{n}}(s_{\mathrm{n}})\left\langle\left.\frac{\partial\overleftrightarrow{\mathbf{G}}\left(\mathbf{r},\mathbf{r}';s\right)}{\partial s}\right|_{s=s_{\mathrm{n}}},\mathbf{J}_{\mathrm{n}}\left(\mathbf{r}'\right)\right\rangle_{\mathbf{r}'}\\&=-\mathbf{E}_{\mathrm{t}}^{\mathrm{inc}}(\mathbf{r};s_{\mathrm{n}})\end{aligned} \tag{2.32}$$

The inner products in the left-hand side of (2.32) are performed on the $\mathbf{r}'$ parameter. Thus, both sides of the equation are functions of $\mathbf{r}$. By taking the inner products of the two sides of (2.32) by $\mathbf{M_n}(\mathbf{r})$, the coupling coefficients can be found at resonant frequencies as

$$R_{\mathrm{n}}(s_{\mathrm{n}}) = -\frac{\left\langle \mathbf{M}_{\mathrm{n}}(\mathbf{r}), \mathbf{E}_{\mathrm{t}}^{\mathrm{inc}}(\mathbf{r}; s_{\mathrm{n}}) \right\rangle_{r}}{\left\langle \mathbf{M}_{\mathrm{n}}(\mathbf{r}), \left\langle \left. \frac{\partial \overleftrightarrow{\mathbf{G}}(\mathbf{r}, \mathbf{r}'; s)}{\partial s} \right|_{s=s_{\mathrm{n}}} , \mathbf{J}_{\mathrm{n}}\left(\mathbf{r}'\right) \right\rangle_{\mathbf{r}'} \right\rangle_{\mathbf{r}}} \tag{2.33}$$

For electric-field integral equations (EFIE), where symmetric matrices are encountered, the coupling vectors and natural mode vectors are the same [33], so that (2.33) is written by

$$R_{\mathrm{n}}(s_{\mathrm{n}}) = -\frac{\left\langle \mathbf{J}_{\mathrm{n}}(\mathbf{r}), \mathbf{E}_{\mathrm{t}}^{\mathrm{inc}}(\mathbf{r}; s_{\mathrm{n}}) \right\rangle_{r}}{\left\langle \mathbf{J}_{\mathrm{n}}(\mathbf{r}), \left\langle \left. \frac{\partial \overleftrightarrow{\mathbf{G}}(\mathbf{r}, \mathbf{r}'; s)}{\partial s} \right|_{s=s_{\mathrm{n}}} , \mathbf{J}_{\mathrm{n}}\left(\mathbf{r}'\right) \right\rangle_{\mathbf{r}'} \right\rangle_{\mathbf{r}}} \tag{2.34}$$

It is seen in (2.34) that the coupling coefficients at resonant frequencies depend on the incident electric field as well as the natural mode distribution at the corresponding resonant frequency. In the cases where $\langle \mathbf{J}_{\mathbf{n}}(\mathbf{r}), \mathbf{E}_{\mathrm{t}}^{\mathrm{inc}}(\mathbf{r}; s_{\mathrm{n}}) \rangle_{\mathbf{r}} = 0$, the related mode will not be excited by the incident electric field. The coupling coefficients in (2.34) are just obtained at CNRs of the tag. There is no straightforward way to obtain the entire function added to the resonant response of the scatterer in (2.23). Mathematically, this is necessary to guarantee convergence of the series. However, more explanation is needed in order to understand the physical concepts behind the theory of SEM.

2.2.2.1 Coupling Coefficients and Turn-On Times

As the equation (2.34) shows, the coupling coefficients at the resonant frequencies of the structure depend on the natural modes, dyadic Green's function of the structure, and incident field at those frequencies. For other complex frequencies, s, different representations can be chosen as the coupling coefficient, which affects the entire function added to the series. In the late-time response of the scatterer, we have just the damped sinusoidals corresponding to the CNRs of the tag. Hence, the entire-function contribution comes into the early-time response, which rises and falls faster than the late-time signals. In order to cover other complex frequencies, different coupling coefficients have been introduced, where class 1 and class 2 representations are most common in literature [33]. For a class 1 representation, which is the simplest one, the coupling coefficients of the natural modes are defined as

$$R_{\mathrm{n}}^{(1)}(s) = e^{(s_{\mathrm{n}}-s)t_0} R_{\mathrm{n}}(s_{\mathrm{n}}) = -e^{(s_{\mathrm{n}}-s)t_0} \frac{\left\langle \mathbf{J}_{\mathrm{n}}(\mathbf{r}), \mathbf{E}_{\mathrm{t}}^{\mathrm{inc}}(\mathbf{r}; s_{\mathrm{n}}) \right\rangle_{\mathbf{r}}}{\left\langle \mathbf{J}_{\mathrm{n}}(\mathbf{r}), \left\langle \left. \frac{\partial \overleftrightarrow{\mathbf{G}}(\mathbf{r}, \mathbf{r}'; s)}{\partial s} \right|_{s=s_{\mathrm{n}}}, \mathbf{J}_{\mathrm{n}}(\mathbf{r}') \right\rangle_{\mathbf{r}'} \right\rangle_{\mathbf{r}}} \tag{2.35}$$

By inserting (2.35) in the series part in (2.23), the time-domain response is given by

$$\mathbf{j}(\mathbf{r}; t) = U(t - t_0)\mathrm{Re}\left[\sum_{n=1}^{\infty} R_{\mathrm{n}} \mathbf{j}_{\mathrm{n}}(\mathbf{r}) e^{s_{\mathrm{n}} t}\right] + \mathbf{j}_{\mathrm{e}}(\mathbf{r}; t) \tag{2.36}$$

where $U(.)$ is the Heaviside step function defined as

$$U(t - t_0) = \begin{cases} 1 & t \geq t_0 \\ 0 & t < t_0 \end{cases} \tag{2.37}$$

and the inverse Laplace transform is defined as

$$\mathbf{j}(\mathbf{r}; t) = \int_{Br} e^{st} \mathbf{J}(\mathbf{r}; s) ds \tag{2.38}$$

which causality ensured by having the Bromwich integration contour Br passing above all singularities in the s-plane. Turn-on time might be the time at which the incident wave is first applied anywhere on the tag. Although class 1 form of the coupling is more useful in the analytical-based formulation of SEM, it shows some convergence issues in earlier times of the response in numerical calculations [36]. For computational purposes, the class 2 form is more efficient. In this form, the frequency dependency of the coupling coefficients is held in the incident electric field as

$$R_{\mathrm{n}}^{(2)}(s) = -\frac{\left\langle \mathbf{J}_{\mathrm{n}}(\mathbf{r}), e^{(s_{\mathrm{n}}-s)t_0} \mathbf{E}_{\mathrm{t}}^{\mathrm{inc}}(\mathbf{r}; s) \right\rangle_{\mathbf{r}}}{\left\langle \mathbf{J}_{\mathrm{n}}(\mathbf{r}), \left\langle \left. \frac{\partial \overleftrightarrow{\mathbf{G}}(\mathbf{r}, \mathbf{r}'; s)}{\partial s} \right|_{s=s_{\mathrm{n}}}, \mathbf{J}_{\mathrm{n}}(\mathbf{r}') \right\rangle_{\mathbf{r}'} \right\rangle_{\mathbf{r}}} \tag{2.39}$$

The effect of these coupling coefficients on the current distribution can be better illustrated in the time domain. For more simplicity, the following incident electric field is considered.

$$\mathbf{E}_{\mathrm{t}}^{\mathrm{inc}}(\mathbf{r}; s) = \mathbf{E}_0 e^{-\frac{s}{c}\hat{\mathbf{r}}.\mathbf{r}} \tag{2.40}$$

where the vector $\hat{r}$ is the propagation vector, $\mathbf{E}_0$ includes the polarization vector and amplitude of the incident wave, and c is the speed of light in free space. By inserting

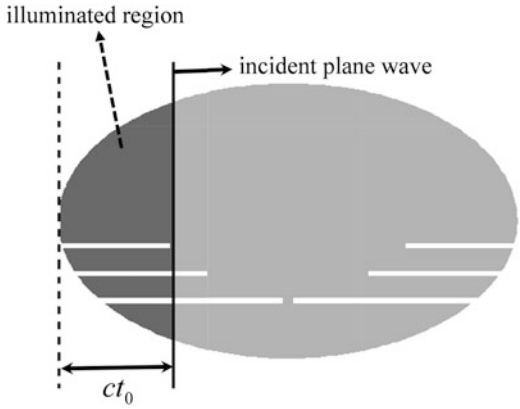

Fig. 2.3 3-bit tag illuminated partly by an incident plane wave

(2.39) and (2.40) in (2.23), the current distribution in the Laplace domain is written as

$$\mathbf{J}(\mathbf{r};s)=\sum_{n=-\infty}^{\infty}\frac{\left\langle \mathbf{J}_{\mathrm{n}}(\mathbf{r}),\mathbf{E}_0 e^{(s_{\mathrm{n}}-s)t_0-\frac{s}{c}\hat{\mathbf{r}}\cdot\mathbf{r}}\right\rangle_{\mathbf{r}}\mathbf{J}_{\mathrm{n}}(\mathbf{r})}{(s-s_{\mathrm{n}})\left\langle \mathbf{J}_{\mathrm{n}}(\mathbf{r}),\left\langle \left.\frac{\partial\overleftrightarrow{\mathbf{G}}(\mathbf{r},\mathbf{r}';s)}{\partial s}\right|_{s=s_{\mathrm{n}}},\mathbf{J}_{\mathrm{n}}(\mathbf{r}')\right\rangle_{\mathbf{r}'}\right\rangle_{\mathbf{r}}}+\mathbf{J}_{\mathrm{e}}(\mathbf{r};s) \quad (2.41)$$

By applying the inverse Laplace transform defined in (2.38) to (2.41), the current distribution in time domain is written as

$$\mathbf{j}(\mathbf{r};t)=2\sum_{n=1}\mathrm{Re}\left(\frac{\left\langle \mathbf{J}_{\mathrm{n}}(\mathbf{r}),\mathbf{E}_0 e^{-\frac{s_{\mathrm{n}}}{c}\hat{\mathbf{r}}\cdot\mathbf{r}}U\left(t-t_0-\frac{\hat{\mathbf{r}}\cdot\mathbf{r}}{c}\right)\right\rangle_{r}\mathbf{J}_{\mathrm{n}}(\mathbf{r})}{\left\langle \mathbf{J}_{\mathrm{n}}(\mathbf{r}),\left\langle \left.\frac{\partial\overleftrightarrow{\mathbf{G}}(\mathbf{r},\mathbf{r}';s)}{\partial s}\right|_{s=s_{\mathrm{n}}},\mathbf{J}_{\mathrm{n}}(\mathbf{r}')\right\rangle_{\mathbf{r}'}\right\rangle_{\mathbf{r}}}e^{s_{\mathrm{n}}t}\right)+\mathbf{j}_{\mathrm{e}}(\mathbf{r};t) \quad (2.42)$$

The convergence difficulties in the class 1 form of coupling coefficients are alleviated in the class 2 representation, where a time-varying region of integration covers that part of the object surface, which has already been illuminated by the incident field [36]. When the incident wave completely passes through the tag, both class 1 and class 2 representations are similar. For better illustration, Fig. 2.3 shows the region of integration at $t=t_0$ on the surface of the tag for class 2 coupling coefficients when the incident plane wave passes through a part of the tag.

2.2.2.2 Scattered Field from Chipless RFID Tags

By representing the current distribution on the tag as the summation over the natural modes in the late-time response accompanying an entire function as the early-time response, the scattered field is obtained from the integral equation in (2.14) as

$$\begin{aligned}\mathbf{E}^{\mathrm{s}}(\mathbf{r};s) &= \left\langle \overleftrightarrow{\mathbf{G}}\left(\mathbf{r},\mathbf{r}';s\right), \sum_n \frac{R_{\mathrm{n}}(s)\mathbf{J}_{\mathrm{n}}\left(\mathbf{r}'\right)}{s-s_n} + \mathbf{J}_{\mathrm{e}}\left(\mathbf{r}';s\right) \right\rangle_{\mathbf{r}'} \\ &= \sum_n \frac{\left\langle \overleftrightarrow{\mathbf{G}}\left(\mathbf{r},\mathbf{r}';s\right), \mathbf{J}_{\mathrm{n}}(s)R_{\mathrm{n}}(s) \right\rangle_{\mathbf{r}'}}{s-s_{\mathrm{n}}} + \left\langle \overleftrightarrow{\mathbf{G}}\left(\mathbf{r},\mathbf{r}';s\right), \mathbf{J}_{\mathrm{e}}\left(\mathbf{r}';s\right) \right\rangle_{\mathbf{r}'}\end{aligned} \tag{2.43}$$

The radiated field close to the nth CNR is written by

$$\mathbf{E}^{\mathrm{s}}(\mathbf{r};s) = \left\langle -\mu s\left(\overleftrightarrow{\mathbf{I}} - \frac{1}{k^2}\nabla\nabla\right) G_0\left(\mathbf{r},\mathbf{r}';s\right), \frac{R_{\mathrm{n}}(s)\mathbf{J}_{\mathrm{n}}\left(\mathbf{r}'\right)}{s-s_{\mathrm{n}}} + \mathbf{J}_{\mathrm{e}}\left(\mathbf{r}';s\right) \right\rangle_{\mathbf{r}'} \tag{2.44}$$

In the far field, the field in (2.44) can be approximated by

$$\begin{aligned}\mathbf{E}_{\mathrm{n}}(\mathbf{r};s) &= \left\langle -\mu s\left(\overleftrightarrow{\mathbf{I}} - \hat{r}\,\hat{r}\right) G_0\left(\mathbf{r},\mathbf{r}'\right), \left.\frac{R_n(s)\mathbf{J}_{\mathrm{n}}\left(\mathbf{r}'\right)}{s-s_{\mathrm{n}}}\right|_{s=s_{\mathrm{n}}} \right\rangle_{\mathbf{r}'} \\ &\quad - \left\langle \mu s\left(\overleftrightarrow{\mathbf{I}} - \hat{r}\,\hat{r}\right) G_0\left(\mathbf{r},\mathbf{r}'\right), \mathbf{J}_{\mathrm{e}}\left(\mathbf{r}';s\right) \right\rangle_{\mathbf{r}'} \\ &= \left\langle -\mu s\left(\overleftrightarrow{\mathbf{I}} - \hat{r}\,\hat{r}\right) \frac{e^{-jk\left(r-r'\cdot\hat{r}\right)}}{4\pi r}, \left.\frac{R_{\mathrm{n}}(s)\mathbf{J}_{\mathrm{n}}\left(\mathbf{r}'\right)}{s-s_{\mathrm{n}}}\right|_{s=s_{\mathrm{n}}} \right\rangle_{\mathbf{r}'} \\ &\quad - \left\langle \mu s\left(\overleftrightarrow{\mathbf{I}} - \hat{r}\,\hat{r}\right) \frac{e^{-jk\left(r-r'\cdot\hat{r}\right)}}{4\pi r}, \mathbf{J}_{\mathrm{e}}\left(\mathbf{r}';s\right) \right\rangle_{\mathbf{r}'}\end{aligned} \tag{2.45}$$

As (2.45) expresses, in the far-field region, the scattered fields in the time domain are approximately proportional to the first derivative of the current distributions on the tag. In contrast, in the near field, the field distribution is mostly affected by the spatial derivatives of the currents. By applying the inverse Laplace transform to the scattered field in (2.43), the fields in the time domain are written as

$$e^{\mathrm{s}}(\mathbf{r};t) = U(t-t_0)\sum_n |R_{\mathrm{n}}| e^{-\alpha_{\mathrm{n}}t}\cos\left(\omega_{\mathrm{n}}t + \phi_{\mathrm{n}}\right) + e_{\mathrm{e}}(\mathbf{r};t) \tag{2.46}$$

where the class 1 form of coupling coefficients is assumed in (2.46). According to (2.46), the scattered field from a tag is affected by two different phenomena. Early-time response, which is depicted by $e_{\mathrm{e}}(r;t)$ in (2.46), is affected by the specular reflections from the scattering centers of the tag. The early-time response is followed by the series of damped sinusoidals with some weighting coefficients. The CNRs of the tag, shown by $s_{\mathrm{n}} = \alpha_{\mathrm{n}} + \mathrm{j}\omega_{\mathrm{n}}$, are aspect-independent parameters of the tag, not dependent on the direction, polarization, or distance to the tag's observation point. For this reason, they are well-suited to be used as the tag's ID. In Chap. 4, different techniques are proposed for extracting the CNRs from the scattered field.

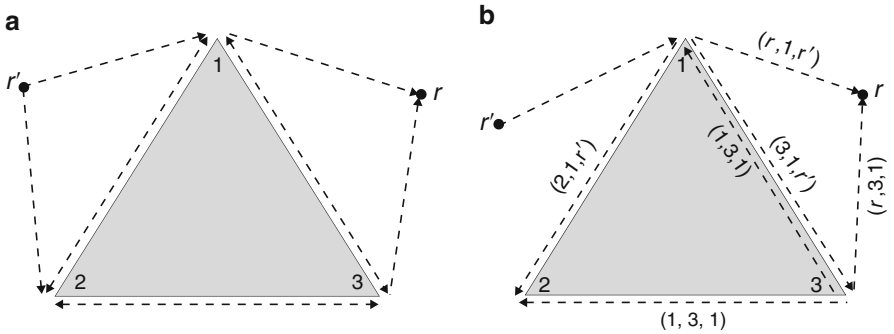

Fig. 2.4 (**a**) Scattering configuration. (**b**) Ray tracing from the source to observation point [37] with permission from IEEE

2.2.2.3 Wavefront Interpretation of the Singularity Expansion Method

As explained in previous sections, the CNRs and corresponding natural modes are aspect-independent parameters, which instead depend on the geometry and material of the tag. In order to ensure convergence of the series in the late time, an entire function was added to the current distribution responsible for the early-time variations. The shape of the entire function in (2.23) is dictated by the coupling coefficient representation chosen in the series. This part is called the removable early-time response [37]. In spite of the mathematical representation in (2.23), there is an intrinsic early-time response, which is related to the scattering process [37]. This part, with fast rise-and-fall variations in the time domain, cannot be described by the oscillatory waves from global CNRs of the tag. Rather, it can be explained by the progressive waves (wavefronts) with the help of the geometrical theory of diffraction (GTD) [37–39]. In the wavefront representation [37], the waves travel from source to tag. At the tag surface, they undergo an interactive process which appears to the observer as a series of wavefront arrivals corresponding to multiple passes through the tag and diffraction from those scattering centers. In [37], a hybrid method based on wavefront interpretation has been presented, which shows the global resonances to be a collective summation of multiple wavefront fields.

As an example, Fig. 2.4a shows a scatterer irradiated by an incident wavefront launched from a source located at r'. Three corners of the scatterer are considered as the scattering centers and the observation point is located at r. The situation shown in Fig. 2.4a is a bistatic situation, which can easily be adopted to the monostatic case by fixing the source and observation points at the same position. When a scatterer is illuminated by a pulse signal, first the specular reflections from the scattering centers are scattered around, emanating from the local current distribution on the discontinuities in the scattering surface. After the incident pulse passes through the scatterer, the local current distributions converge to the natural current modes of the scatterer, which are responsible for the late-time response. In other words, the interaction between local resonances in the early time produces the global complex natural

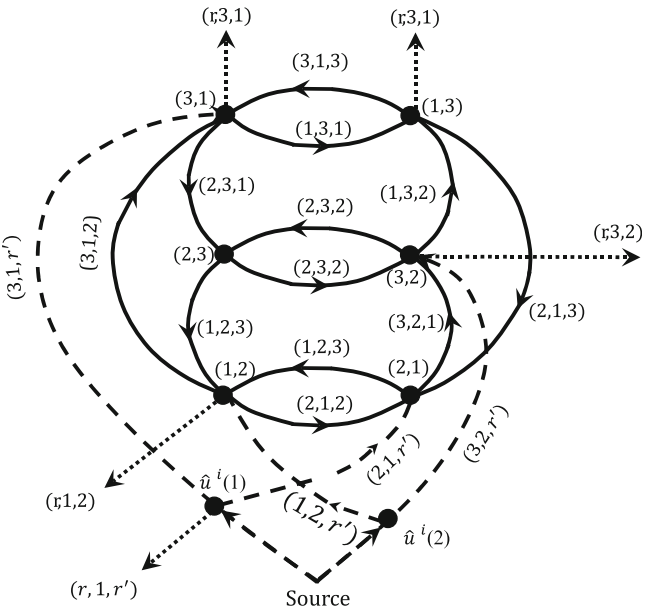

Fig. 2.5 Flow graph of the scatterer [37] with permission from IEEE

resonances of the scatterer. This behavior is illustrated in Fig. 2.4b. Two different rays are traced from the source point to the scatterer. Each path is illustrated by three components, (r_1, r_2, r_3), which express the field at the point r_1 caused by scattering at r_2 of a ray field with unit amplitude arriving from a point r_3.

In Fig. 2.4b, the incident ray hits the first scattering center. Part of it is received at the observation point via $(r, 1, r')$ and the other part flows to corner 3 through $(3, 1, r')$. Again, part of the ray in corner 3 hits the observation point through $(r, 3, 1)$ and the other part travels to the second corner by (2, 3, 1), and the third part reflects back to the first corner through (1, 3, 1). There is a local resonance in the path between corners 1 and 2. The other diffracted rays from the scattering centers are traced in the same way as mentioned before. This ray interaction can be easily traced with a signal flow graph, shown in Fig. 2.5. The rays scattered to the observation point are shown by dashed lines. For time-harmonic ray fields, a ray has the local plane-wave form of

$$S(r_1, r_2, r_3) \sim A(r_1, r_2, r_3)\exp[jk\psi(r_1, r_2, r_3)] \tag{2.47}$$

where A and $k\psi$ are slowly-varying amplitude and rapidly-varying phase functions, respectively. From the flow graph seen in Fig. 2.5, the ray paths from source to observation point can be divided into two groups. The first group, shown with a dashed line, contains contributions at r from direct interaction of the incident field with each of the scattering centers, which are shown by $\hat{u}^i(j)$, $j = 1, 2, 3$ in Fig. 2.5.

The summation of these terms with weighting functions proportional to (2.47) includes the intrinsic early-time response of the scatterer caused by the scattering process. The second group accounts cumulatively for all the higher-order interactions schematized by the solid branches in the graph. This part of the response represents the SEM resonances of the scatterer. By returning to the general problem, scattered signal at the observation point can be written with Mason's formula as

$$u(r) = \sum_n u_{\mathrm{n}}^{\mathrm{d}} + \frac{1}{\Delta}\sum_n u_{\mathrm{n}}^{\mathrm{w}}\Delta_{\mathrm{n}} \tag{2.48}$$

where the first term is responsible for the early-time response and contains the direct interactions of the incident ray field with scattering centers. The second term, the late-time component of the response, represents the coupling between different local resonances on the surface of the scatterer. The quantity $u_{\mathrm{n}}^{\mathrm{d}}$ is the direct nth path from source to the observation point (shown by dashed lines in Fig. 2.5) and $u_{\mathrm{n}}^{\mathrm{w}}$ represents the wavefront contribution along paths going from source to observer via successive (more than one but without repetition) single scattering events. Δ_{n} shows the gain of the non-touching closed loops having no interaction with $u_{\mathrm{n}}^{\mathrm{w}}$, and Δ is the characteristic determinant of the graph. The zeroes of Δ are the CNRs of the scatterer. Although the wavefront representation of the scattering process cannot easily be employed for calculating the early-time and late-time responses of the tag, it provides a descriptive model for the scattering mechanism.

2.2.2.4 Altes' Model

Though the late-time response of the tag can be compactly cast into a series-form formulation, it is not as easy to predict the behavior of the early-time response. This is because it depends on the spatial variations of the scatterer and observation point. Based on (2.43), the early-time response is formulated by

$$\mathbf{E}_{\mathrm{e}}(r;s) = \left\langle -\mu s\left(\overleftrightarrow{\mathbf{I}} - \frac{1}{k^2}\nabla\nabla\right)G_0\left(\mathbf{r},\mathbf{r}';s\right), \mathbf{J}_{\mathrm{e}}\left(\mathbf{r}';s\right)\right\rangle \tag{2.49}$$

where the first part of the dyadic Green's function is more pronounced in the far zone and the second term is dominant in the near zone of the scatterer. Because of the fast variations of the early-time currents, the scattered field includes pulse-shape impulses reflected from the scattering centers of the tag. Assuming a scatterer containing M scattering centers is illuminated by an incident plane wave with pulse function $p(t)$, the backscattered signal in the early time can be modeled as the summation of the delayed pulses from the scattering centers as [40]

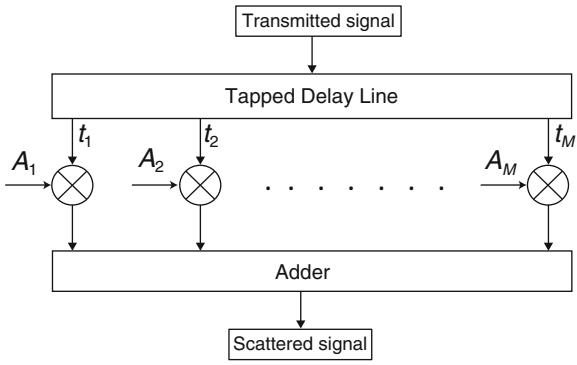

Fig. 2.6 Transversal filter model of the early-time response [40]

$$e_{\mathrm{e}}(r;t) = \sum_{m=1}^{M} A_{\mathrm{m}} p(t - t_{\mathrm{m}}) \tag{2.50}$$

where A_{m} and t_{m} are the amplitude and time delay related to the mth scattering center. This early-time representation is modeled in Fig. 2.6 as a tapped delay line (t_1, t_2, …, t_{M}) with M multipliers and an adder. This model is compatible with the wavefront representation exhibited in Sect. 2.2.2.3. It was shown that the early-time response emanates from the first interaction of the incident pulse with the scattering centers of the tag, as (2.50) describes.

Based on physical optics approximations, some functions other than impulses must be added to the series in (2.50) in order to completely model the early-time response of the scatterer [40]. The model seen in Fig. 2.7, which includes the parallel combinations of the integrators and differentiators, can be described with the well-accepted model in Fig. 2.6 by assuming that some of the delay differences $t_{\mathrm{m+1}} - t_{\mathrm{m}}$ are very small compared to the smallest wavelength of the impinging signal. If two neighboring scattering centers in Fig. 2.6 have opposite signs, and their delay difference ($d = t_{\mathrm{m+1}} - t_{\mathrm{m}}$) is very small, $d \ll 1$, one can write

$$A_{\mathrm{m}}(p(t - t_{\mathrm{m+1}}) - p(t - t_{\mathrm{m}})) \propto \left.\frac{dp(t)}{dt}\right|_{t=t_{\mathrm{m}}} \tag{2.51}$$

This component is proportional to the differentiated signal at $t = t_m$. Similarly, weighting factors can result in a return component as

$$[p(t) + p(t+d) + \cdots + p(t+kd)] \propto \int_0^{kd} p(t)dt \tag{2.52}$$

In order to perfectly model the early-time response of the scatterer, one must consider both the integrators and differentiators in the model, in addition to the replica of the incident pulse. This model is formulated as the convolution of the incident pulse with the impulse responses of the scattering centers.

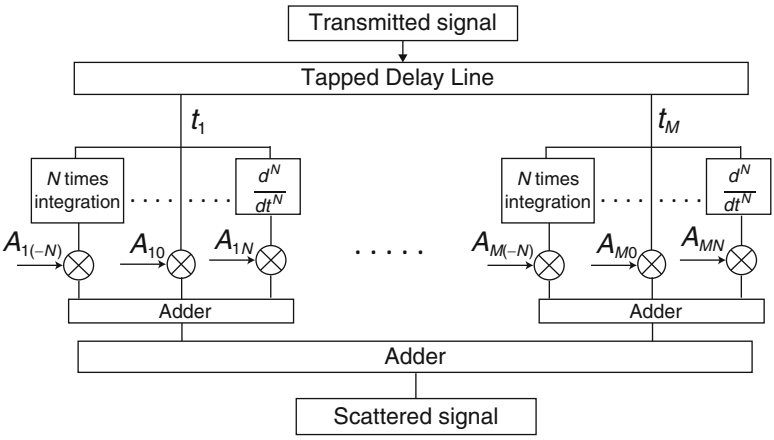

Fig. 2.7 Modified Transversal filter model of the early-time response [40]

$$e_{\mathrm{e}}(r;t) = p(t) * \sum_{m=1}^{M} \sum_{n=-\infty}^{+\infty} A_{\mathrm{mn}} \delta^{(n)}(r; t - t_{\mathrm{m}}) \tag{2.53}$$

In (2.53), the impulse response of the mth scattering center is summed over the integrals and derivatives of the Dirac-delta function. Here, the negative and positive values of n refer to the nth integral and derivative of the delta function with respect to time. In the Laplace domain, the early-time response is written by

$$\begin{aligned} E_{\mathrm{e}}(r;s) &= \sum_{m=1}^{M} \sum_{n=-\infty}^{+\infty} A_{\mathrm{mn}} s^n P(r;s) e^{st_{\mathrm{m}}} \\ &= \sum_{m=1}^{M} \sum_{n=-\infty}^{+\infty} B_{\mathrm{mn}}(r;s) e^{st_{\mathrm{m}}} \end{aligned} \tag{2.54}$$

where

$$B_{\mathrm{mn}} = A_{\mathrm{mn}} s^n P(r;s) \tag{2.55}$$

By comparing (2.54) with (2.46), it is inferred that there is a duality between early-time response in the Laplace domain and late-time response in the time domain. In the former, the response is expanded over the exponential functions of delay times, while in the latter, the time-domain response is expanded versus exponential functions of complex resonances of the tags. This duality will be helpful in the identification process of chipless RFID tags, presented in Chap. 5.

In simple scatterers such as chipless RFID tags, the reflection from the first illuminated part of the tag is strong enough to be considered as the early-time response of the tag. But in the complex scatterers such as an airplane, the impulse responses of the multiple scattering centers of the target should be considered in

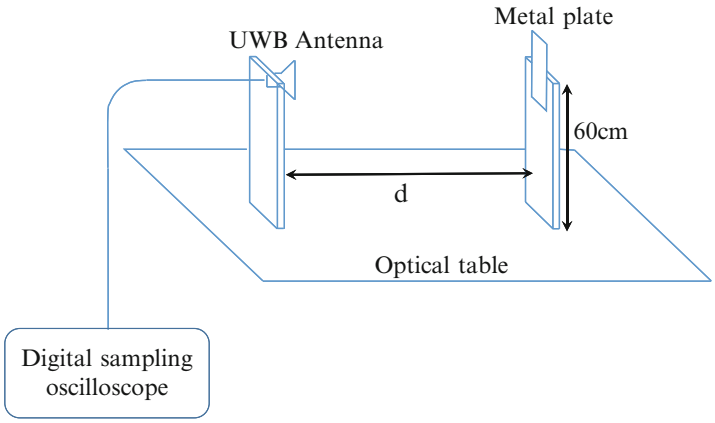

Fig. 2.8 Measurement setup to measure a UWB pulse scattered from a metal object

the response. Therefore, the early-time response from the simple scatterers can accurately be approximated by just one term of the series shown in (2.53). This part is strongly dependent on the polarization and direction of the incident electric field. This is because of the dependency of the scattering centers on the polarization and direction of the incident wave. Additionally, the shape of the early-time response changes from the near field of the scatterer to its far field.

In the near field, the scattered field is mostly similar to the incident pulse, but in the far field, the scattered field is limited to the first time-derivative of the incident field [41].

As an example, the scattered field from a rectangular metal plane with size of 15 cm $\times$ 15 cm illuminated by an incident pulse is considered. The measurement set-up is shown in Fig. 2.8. A rectangular metal plane is located 60 cm above an optical table. A TEM horn antenna is connected to a digital sampling oscilloscope in order to calculate the backscattered signal from the tag at different distances. Another measurement without the presence of the metal is performed and the results are subtracted from the earlier signal to cancel the effects of background objects. Time averaging is applied to the received pulses in order to improve the signal-to-noise ratio (SNR). The excitation pulse and its derivative with respect to time are shown in Fig. 2.9. In Fig. 2.10, the backscattered signal from the plate is shown when it is located at four different distances $d = 20$ cm, 30 cm, 1 m and 1.3 m away from the antenna aperture. In the cases where $d = 20$ cm and 30 cm, the observation point is in the near-field of the scatterer and as can be seen, the scattered signal is similar to the incident pulse. In these two cases, the scattered signal is followed by a tail, which is related to the impulse response of the antenna. By locating the plate and the antenna in the far-field of each other, the scattered signal inclines to the first derivative of the incident pulse. By increasing the distance between the antenna and scatterer, the amplitude of the scattered signal decreases. In Fig. 2.11, the normalized responses are plotted for $d = 20$ cm and $d = 130$ cm. According to the results, the scattered field is similar to the incident field in the

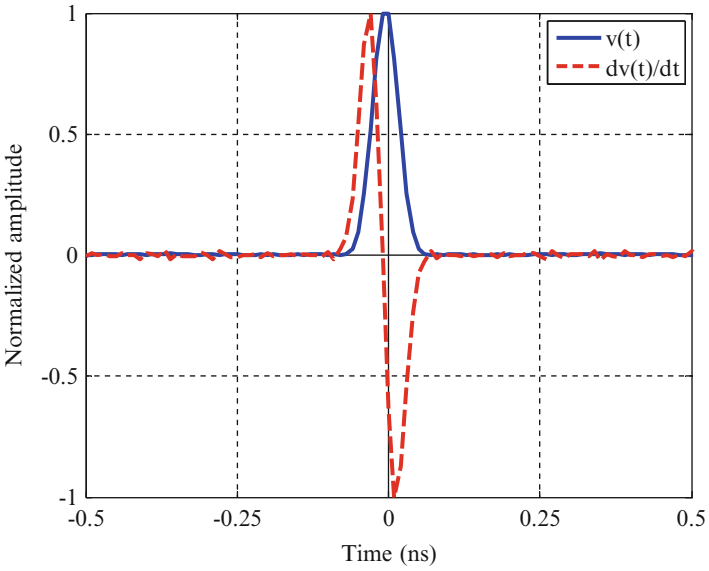

Fig. 2.9 Excitation pulse and its derivative with respect to time

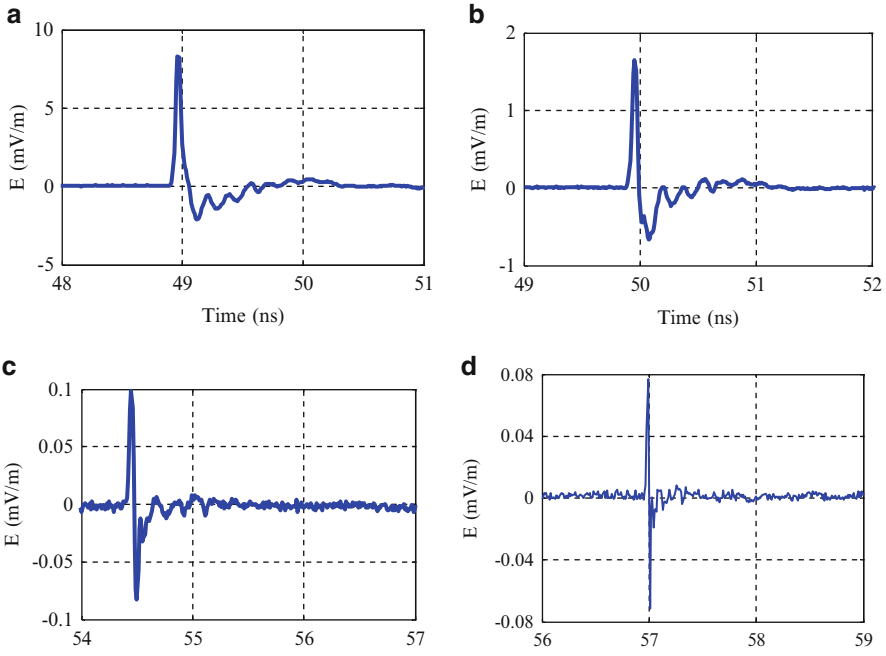

Fig. 2.10 Received electric field from the metal object for different distances (**a**) d = 20 cm, (**b**) d = 30 cm, (**c**) d = 100 cm, and (**d**) d = 130 cm

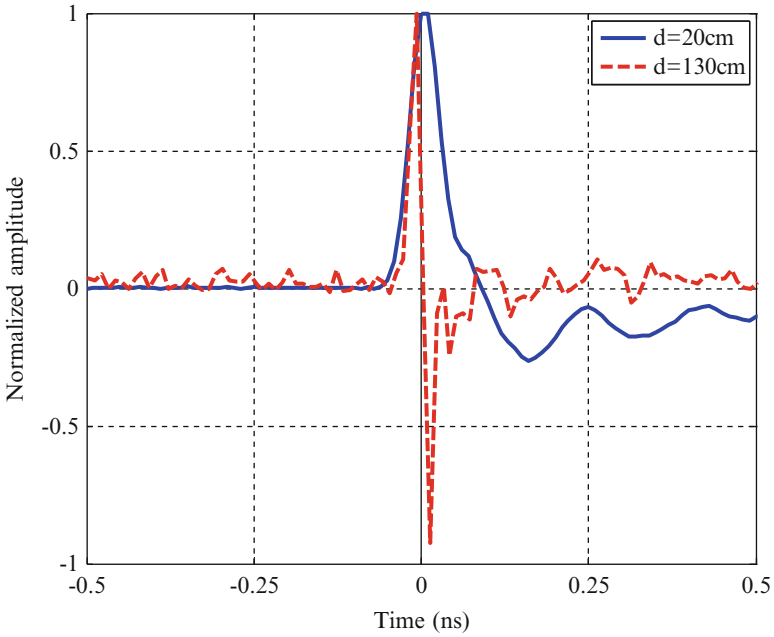

Fig. 2.11 Received electric field from the metal plate for d = 20 cm and d = 130 cm

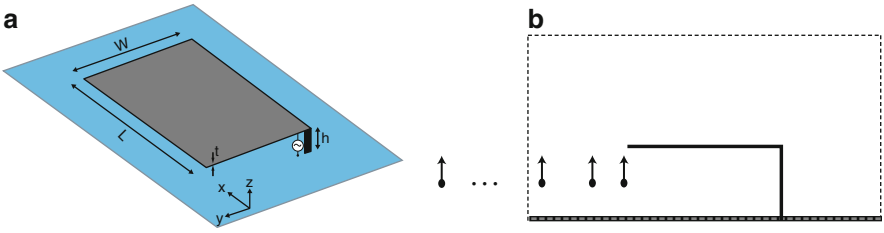

Fig. 2.12 (**a**) 3D view of PIFA antenna (L = 9 mm, W = 5 mm, h = 0.5 mm). (**b**) Cross-section of the antenna and probe located at different distances of the antenna [29] with permission from IEEE

near-field and similar to the first derivative of the incident pulse in the far-field of the scatterer.

This phenomenon also happens in the radiation fields from the antennas. In Fig. 2.12, the 3D view of the planar inverted-F antenna (PIFA) is observed with multiple probes located 1 mm, 10 mm, 30 mm, and 2 m away from the radiating aperture of the antenna. The input signal is a Gaussian pulse with $\tau_{FWHM} = 100ps$ [29]. Figure 2.13 shows the z-component of the radiated fields from the antenna at different probes. As it shows, the early-time response is followed by some sinusoidal signals corresponding to the CNRs of the antenna. Regardless of the probe position at which fields are computed, there are some higher-order resonances at the beginning of all time-domain responses. Each high-order CNR has a unique

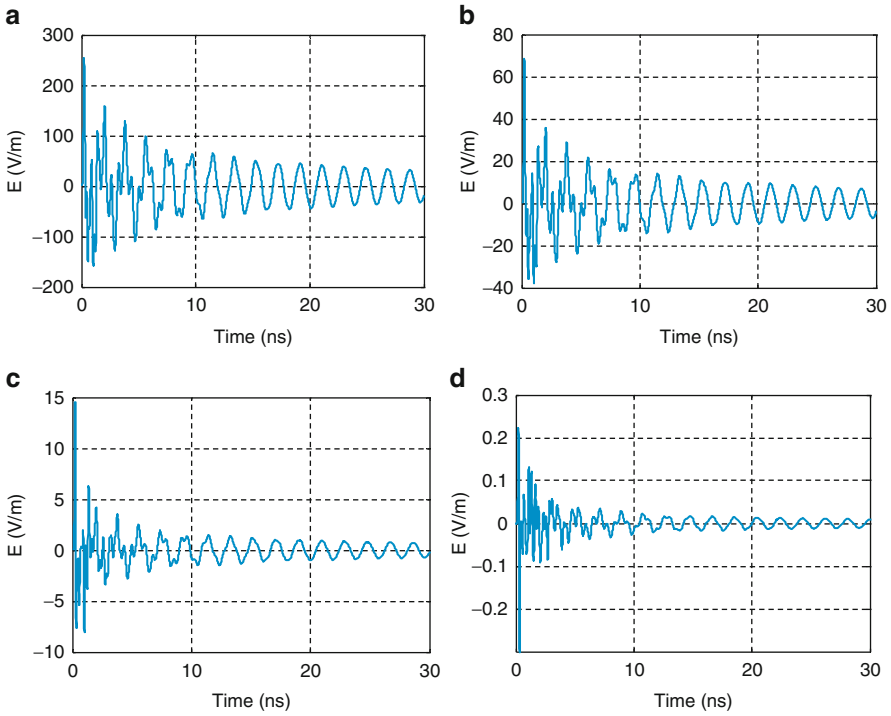

Fig. 2.13 Electric fields received through the probes located at different positions. (**a**) 1 mm (**b**) 10 mm (**c**) 30 mm and (**d**) 2 m [29] with permission from IEEE

damping factor, which is much larger than that of the fundamental mode in this example. Therefore, the effect of the fundamental natural mode is dominant in later times. In Fig. 2.14, the normalized early-time response of the antenna at the probes is depicted. As it shows, at the first probe, located close to the antenna aperture, the electric field is similar to the input pulse. Then by moving farther from the antenna aperture, the shape of the electric field inclines to the first derivative of the input pulse with respect to time [29].

2.2.3 SEM-Based Equivalent Circuit of the Scatterer

In Sect. 2.2.2, the mathematical representation of the scattering process was studied. The early-time response of the scatterer was formulated in (2.53) by the time convolution of the incident pulse with the summation over localized impulse responses of the scattering centers of the tag.

Based on the wavefront method proposed in Sect. 2.2.2.3, the interactions between the local resonances in the early time generate global resonances. According to the singularity expansion method, these global resonances are modeled in the time domain as the summation over damped sinusoidals

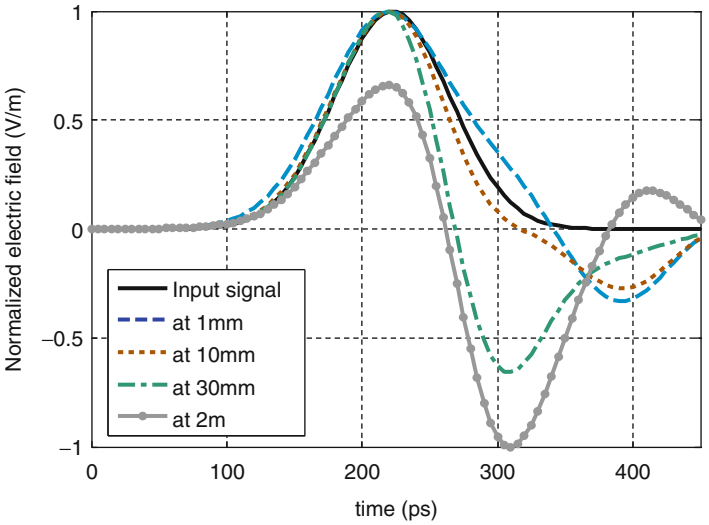

Fig. 2.14 The early-time response of the scatterer received at different probes [29] with permission from IEEE

corresponding to the complex natural resonances of the scatterer with some weighting residues as the coupling coefficients. Although the CNRs are aspect-independent, depending only on the geometry and material of the scatterer, the coupling coefficients are strongly aspect-dependent.

In the scattering analysis, it is usually more desirable to model the scattering process with an equivalent-circuit representation. This equivalent circuit is helpful in the design process of the scatterer. In order to consider the effects of polarization in the scattering process, a general situation, shown in Fig. 2.15, is assumed. Assuming the incident and scattered electric fields as E^{inc} and E^{s} with polarization vectors $\hat{a}_{inc}$ and $\hat{a}_s$, the scattering transfer function of the tag is defined as

$$H_{\text{t}}(\hat{a}_{\text{inc}}, \hat{a}_{\text{s}}; s) = \frac{E^{\text{s}}(r; s)}{E^{\text{inc}}(r; s)} \tag{2.56}$$

Assuming the incident electric field as a Dirac-delta function, the transfer function of the tag is related to the scattered electric field. The equivalent circuit of the tag, shown in Fig. 2.15, is depicted in Fig. 2.16. The input and output voltages are defined at the transmitting and receiving antenna ports, respectively. The incident field is coupled to the CNRs by coupling coefficients $n_{\text{inc}}^{(\text{i})}$ $i = 1, 2, \ldots, N$, which depend on the direction and polarization of the incident electric field.

Each CNR is represented by a parallel RLC circuit in series with a delay line, which models the turn-on times of the CNRs. The excited natural current modes are coupled to the scattered field with coupling coefficients $n_{\text{s}}^{(\text{i})}$ $i = 1, 2, \ldots, N$. The quantity Z_e represents the early-time response of the tag, which is aspect-dependent. The transfer function of the tag as defined in (2.56) is converted to the ratio of

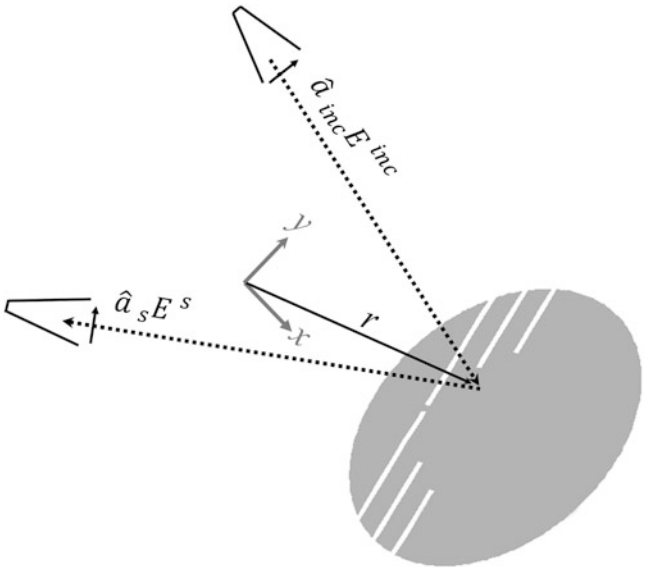

Fig. 2.15 A tag illuminated by an incident wave

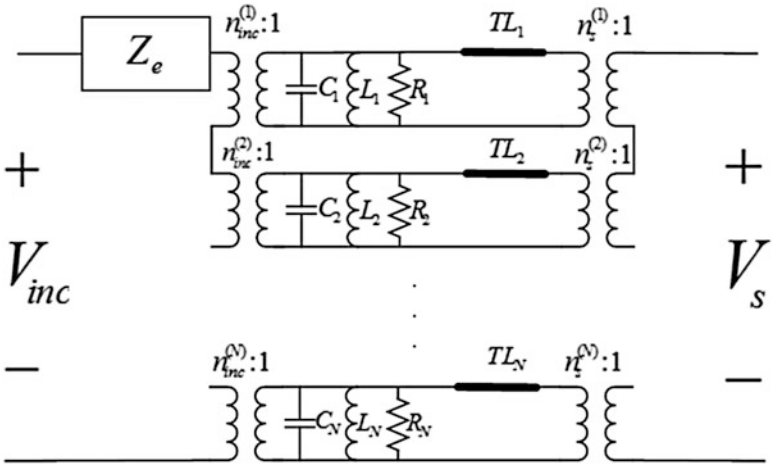

Fig. 2.16 SEM-based equivalent circuit of chipless RFID tag

output to input voltages. With some mathematical manipulation, the transfer function can easily be written as

$$\begin{aligned} H(s) &= H_{\mathrm{e}}(s) + H_{\mathrm{l}}(s) \\ &= H_{\mathrm{e}}(s) + \sum_{n=1}^{N}\left[\frac{A_{\mathrm{n}}}{s - s_n} + \frac{A_n{}^*}{s - s_n{}^*}\right] \end{aligned} \tag{2.57}$$

The first term is the early-time part of the tag and the second term, including the complex natural resonances, is the late-time part. Although in reality, N is infinity, for numerical computations, N is usually truncated to a finite value.

2.2.4 Example: Scattering from a Dipole

In this section, scattered fields from a dipole are formulated based on the SEM in order to illustrate the application of the SEM in numerical computations [42]. A single dipole of length L is aligned with the z-axis and illuminated by an incident plane wave propagating in the direction forming an angle θ with the z-axis. The incident wave is assumed to be a step function, striking the scatterer at $t=0$. By formulating the current distribution using the SEM, it is possible to obtain the current distribution and scattered fields in the time domain. By neglecting the effects of the end caps on the wire and φ variations of the currents on the wire, a Pocklington equation can be written for the axially-directed current on the dipole. Assuming $s=\alpha+\mathrm{j}\omega$, the Pocklington equation is written as [42]

$$-s\varepsilon_0 E_{\mathrm{t}}^{\mathrm{inc}}(z,s)=\int_{-L/2}^{L/2} I\left(z',s\right)\left(\frac{\partial^2}{\partial z^2}-\frac{s^2}{c^2}\right)K\left(z,z';s\right)dz' \tag{2.58}$$

where $E_{\mathrm{t}}^{\mathrm{inc}}$ is the tangential component of the incident electric field along the dipole and the kernel K is given by

$$K\left(z,z';s\right)=\frac{1}{2\pi a}\int_0^{2\pi}\frac{\exp(-sR/c)}{4\pi R}ad\phi \tag{2.59}$$

Here, a is the radius of the wire and

$$R=\left[\left(z-z'\right)^2+4a^2\sin^2(\varphi/2)\right]^{1/2} \tag{2.60}$$

The incident tangential electric field along the dipole is written by (Fig. 2.17)

$$E_t^{inc}(z,s)=E^{inc}(s)\cos(\theta)\exp\left(\frac{sz\sin(\theta)}{c}\right) \tag{2.61}$$

For the step-function incident wave, we have

$$E^{inc}(s)=\frac{E_0}{s} \tag{2.62}$$

By discretizing the length of the dipole into N segments, the integral equation in (2.58) is converted to the equation

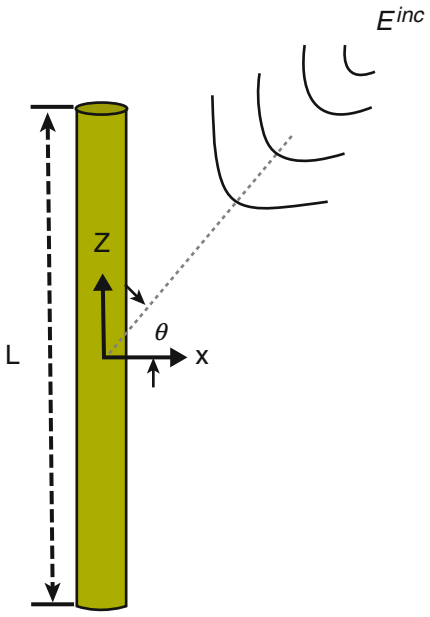

Fig. 2.17 Geometry of the dipole illuminated by an incident field [42] with permission from IEEE

$$[Z][I] = [V] \tag{2.63}$$

where $[Z]$ is an $N \times N$ matrix referred to as the system impedance matrix, $[I]$ is an $N \times 1$ response vector and $[V]$ is an $N \times 1$ vector corresponding to the incident field. According to (2.30), at CNRs of the scatterer, the following equation holds

$$[Z(s_n)][I(s_n)] = 0 \tag{2.64}$$

The CNRs of the dipole are obtained from

$$\Delta(s_n) = \det(Z(s_n)) = 0 \tag{2.65}$$

The CNRs can be calculated by employing different searching algorithms. One easy way is to expand $\Delta(s)$ in a complex Taylor series about s_n as [42]

$$\Delta(s_n) = \Delta(s_0) + \Delta^{'}(s_0)(s - s_0) + \cdots = 0 \tag{2.66}$$

Keeping the first two terms of the series, the CNR, s_n, is obtained from

$$s_n = s_0 - \frac{\Delta(s_0)}{\Delta^{'}(s_0)} \tag{2.67}$$

where s_0 is the initial guess of the resonant frequency. More accurate values for s_n can be obtained by repeating this procedure. Figure 2.18 shows the pole diagram of

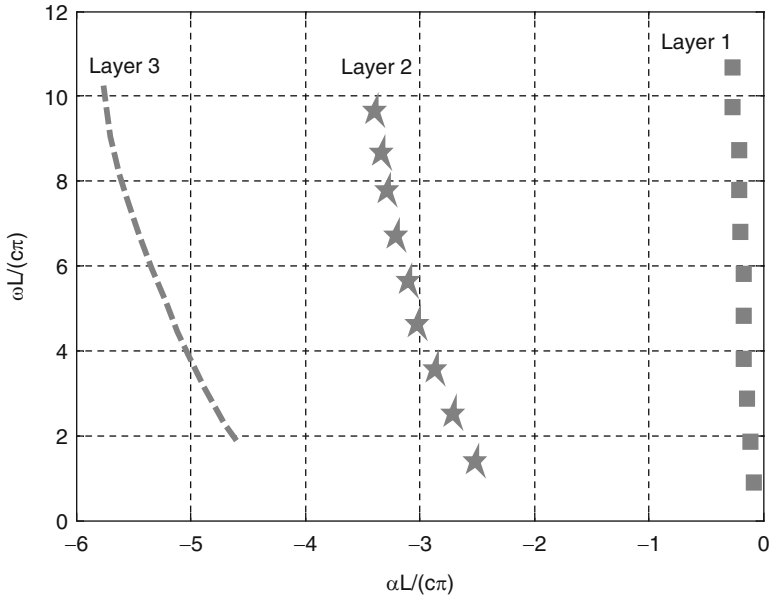

Fig. 2.18 Pole diagram of the dipole, representing the resonant frequency and damping factor of the CNRs [42] with permission from IEEE

the dipole normalized to $c\pi/L$. It is seen that the poles, $s_n = \alpha_n + j\omega_n$, are located in different layers in the s-plane. The poles situated in the first layer are more dominant in the time-domain response because they have lower damping factors than those located in the further layers. The natural current modes on the dipole are the solutions of equation (2.63).

$$[I] = [Z]^{-1}[V] = \frac{[Y]}{\Delta(s)}[V] \tag{2.68}$$

In Fig. 2.19, the real and imaginary parts of the first three modes of the dipole located in the first layer are depicted.

By possessing the natural modes and CNRs of the dipole, the current distribution can be cast to the form

$$[I] = \sum_n \frac{R_n}{s - s_n}[J_n] \tag{2.69}$$

where R_n is the residue of the nth pole, obtained from (2.34). The time-domain response is obtained by applying an inverse Laplace transform along the appropriate Bromwich contour.

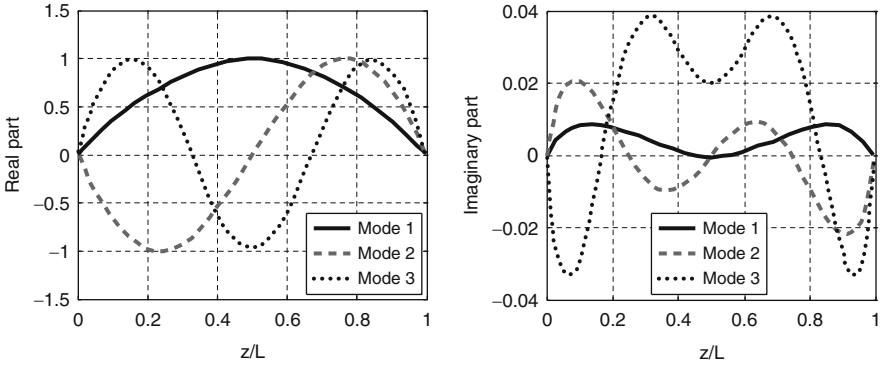

Fig. 2.19 Real and imaginary parts of the first three natural currents of the dipole [42] with permission from IEEE

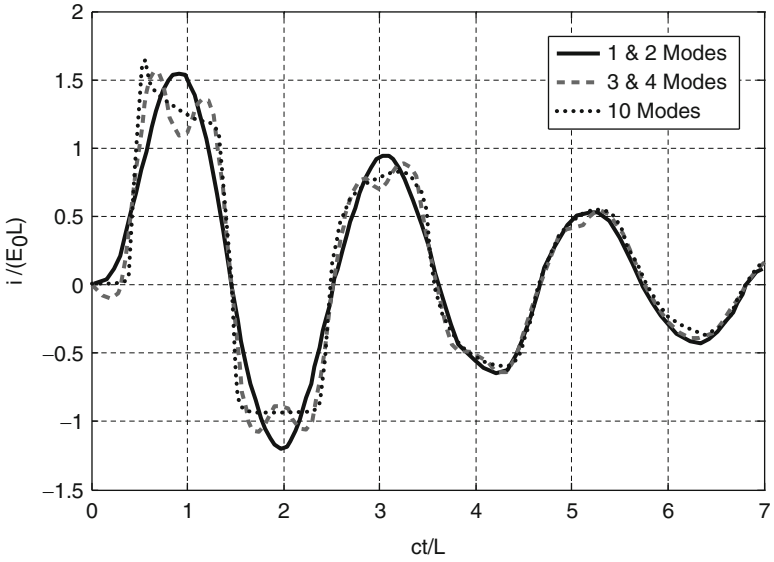

Fig. 2.20 Current distribution at z/L = 0.5 as a function of time [42] with permission from IEEE

$$[i(t)] = \sum_n R_n \exp(s_n t)[J_n] \tag{2.70}$$

We consider the case where the incident electric field propagates in the direction forming $\theta = 30^\circ$ with the dipole. The current at $z/L = 0.5$ is shown in Fig. 2.20 for different numbers of modes considered in the summation. Here, just the poles in the first layer are considered. The effect of high-order resonances is clearly seen in the time-domain response of the dipole. Since in this case, by increasing the order of the resonant mode, its damping factor increases, we can infer that its effect is dominant in earlier times of the response.

2.3 Eigenmode Expansion Method

In the previous section, the scattered fields from the tag were expanded versus the singularities of the structure. Another way of representing the scattered fields from the scatterer is to expand the fields or currents versus the eigenmodes of the structure under consideration. The question may arise of how to extract the singularity poles of the scatterer from the eigenmode expansion of the fields. Before starting the general formulation of the scattered fields from an arbitrary scatterer, a simple case shown in Fig. 2.21 is considered. An ideal dipole is located in a hollow rectangular cavity resonator. In the case shown in Fig. 2.21, the eigenmodes of the structure are easily written in a closed form. By calculating the dyadic Green's function of the structure, the scattered fields are obtained from (2.14). The electric and magnetic fields in the cavity satisfy the following equations

$$\nabla \times \nabla \times \mathbf{E} - k^2 \mathbf{E} = -j\omega\mu \mathbf{J} \tag{2.71}$$

$$\nabla \times \nabla \times \mathbf{H} - k^2 \mathbf{H} = \nabla \times \mathbf{J} \tag{2.72}$$

with the following boundary conditions on the walls.

$$\hat{n} \times \mathbf{E} = 0 \tag{2.73}$$

$$\hat{n} \cdot \mathbf{H} = 0 \tag{2.74}$$

Quantity $\hat{n}$ indicates the direction normal to the wall surfaces. In order to solve the preceding boundary-value problem, two quantities, the electric-type dyadic

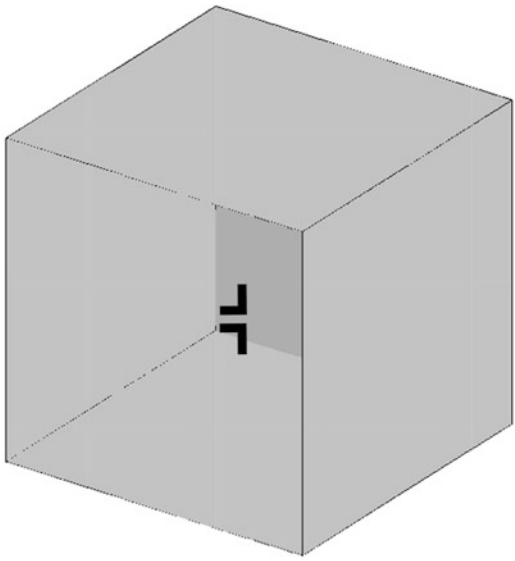

Fig. 2.21 An ideal dipole in a rectangular cavity resonator

Green's function, $\overleftrightarrow{\mathbf{G}}_{\mathrm{e}}$, and the magnetic-type dyadic Green's function, $\overleftrightarrow{\mathbf{G}}_{\mathrm{m}}$, are defined as [43]

$$\nabla \times \nabla \times \overleftrightarrow{\mathbf{G}}_{\mathrm{e}} - k^2 \overleftrightarrow{\mathbf{G}}_{\mathrm{e}} = \overleftrightarrow{\mathbf{I}} \delta\left(\mathbf{r} - \mathbf{r}'\right) \tag{2.75}$$

$$\nabla \times \nabla \times \overleftrightarrow{\mathbf{G}}_{\mathrm{m}} - k^2 \overleftrightarrow{\mathbf{G}}_{\mathrm{m}} = \nabla \times \overleftrightarrow{\mathbf{I}} \delta\left(\mathbf{r} - \mathbf{r}'\right) \tag{2.76}$$

with the following boundary conditions on the walls

$$\hat{n} \times \overleftrightarrow{\mathbf{G}}_{\mathrm{e}} = 0 \tag{2.77}$$

$$\hat{n} \cdot \overleftrightarrow{\mathbf{G}}_{\mathrm{m}} = 0 \tag{2.78}$$

The quantity $\overleftrightarrow{\mathbf{I}}$ in (2.75) and (2.76) is the unit dyad. It is interesting to note that the following relation holds between $\overleftrightarrow{\mathbf{G}}_{\mathrm{e}}$ and $\overleftrightarrow{\mathbf{G}}_{\mathrm{m}}$ [44]

$$k^2 \overleftrightarrow{\mathbf{G}}_{\mathrm{e}} = \nabla \times \overleftrightarrow{\mathbf{G}}_{\mathrm{m}} - \overleftrightarrow{\mathbf{I}} \delta\left(\mathbf{r} - \mathbf{r}'\right) \tag{2.79}$$

From (2.75) and (2.76), it is clear that $\nabla \cdot \overleftrightarrow{\mathbf{G}}_{\mathrm{e}} \neq 0$ and $\nabla \cdot \overleftrightarrow{\mathbf{G}}_{\mathrm{m}} = 0$, while the cavity modes are divergenceless. Therefore, the magnetic dyadic Green's function can be expanded versus cavity modes, and by using the relation in (2.79), the electric dyadic Green's function is obtained. From $\nabla \cdot \overleftrightarrow{\mathbf{G}}_{\mathbf{m}} = 0$ and $\nabla \times \nabla \times = \nabla \nabla \cdot - \nabla^2$, the following alternative form of (2.76) is obtained.

$$\left(\nabla^2 + k^2\right) \overleftrightarrow{\mathbf{G}}_{\mathrm{m}} = -\nabla \times \overleftrightarrow{\mathbf{I}} \delta\left(\mathbf{r} - \mathbf{r}'\right) \tag{2.80}$$

$$\left.\begin{aligned} \hat{n} \cdot \overleftrightarrow{\mathbf{G}}_{\mathrm{m}} &= 0 \\ \hat{n} \times \nabla \times \overleftrightarrow{\mathbf{G}}_{\mathrm{m}} &= 0 \end{aligned}\right\} \text{on the wall} \tag{2.81}$$

By defining another Green's function as

$$\left(\nabla^2 + k^2\right) g_{\mathrm{m}} = -\mathbf{I} \delta\left(\mathbf{r} - \mathbf{r}'\right) \tag{2.82}$$

$$\left.\begin{aligned} \hat{n} \cdot g_{\mathrm{m}} &= 0 \\ \hat{n} \times \nabla \times g_{\mathrm{m}} &= 0 \end{aligned}\right\} \text{on the walls} \tag{2.83}$$

and applying Green's theorem, we have

$$\overleftrightarrow{G}_{\mathrm{m}}\left(r,r^{'}\right)=\int g_{\mathrm{m}}\left(r,r^{''}\right)\cdot\nabla^{''}\times\mathbf{I}\delta\left(r^{'}-r^{''}\right)ds^{''} \tag{2.84}$$

Where ∇'' is differentiation versus r''. Therefore, the components of the dyadic function in (2.82) can be written in the following form

$$\left(\nabla^2+k^2\right)\begin{Bmatrix} g_{\mathrm{m}}^{\mathrm{xx}} \\ g_{\mathrm{m}}^{\mathrm{yy}} \\ g_{\mathrm{m}}^{\mathrm{zz}} \end{Bmatrix}=-\begin{Bmatrix} 1 \\ 1 \\ 1 \end{Bmatrix}\delta\left(\mathbf{r}-\mathbf{r}^{'}\right) \tag{2.85}$$

By expanding the dyadic components versus cavity modes and applying boundary conditions, one can obtain

$$\begin{aligned} g_{\mathrm{m}}\left(r,r^{'}\right)=&\sum_{n=0}^{\infty}\sum_{m=0}^{\infty}\sum_{l=0}^{\infty}\frac{\varepsilon_{0\mathrm{n}}\varepsilon_{0\mathrm{m}}\varepsilon_{0\mathrm{l}}}{abc\left[k^2-\left(\frac{n\pi}{a}\right)^2-\left(\frac{m\pi}{b}\right)^2-\left(\frac{l\pi}{c}\right)^2\right]}\cdot \\ &\left\{\hat{x}\,\hat{x}\left(\sin\left(\frac{n\pi x}{a}\right)\sin\left(\frac{n\pi x^{'}}{a}\right)\cos\left(\frac{m\pi y}{b}\right)\cos\left(\frac{m\pi y^{'}}{b}\right)\cos\left(\frac{l\pi z}{c}\right)\cos\left(\frac{l\pi z^{'}}{c}\right)\right)\right. \\ &+\hat{y}\,\hat{y}\left(\cos\left(\frac{n\pi x}{a}\right)\cos\left(\frac{n\pi x^{'}}{a}\right)\sin\left(\frac{m\pi y}{b}\right)\sin\left(\frac{m\pi y^{'}}{b}\right)\cos\left(\frac{l\pi z}{c}\right)\cos\left(\frac{l\pi z^{'}}{c}\right)\right) \\ &\left.+\hat{z}\,\hat{z}\left(\cos\left(\frac{n\pi x}{a}\right)\cos\left(\frac{n\pi x^{'}}{a}\right)\cos\left(\frac{m\pi y}{b}\right)\cos\left(\frac{m\pi y^{'}}{b}\right)\sin\left(\frac{l\pi z}{c}\right)\sin\left(\frac{l\pi z^{'}}{c}\right)\right)\right\} \end{aligned} \tag{2.86}$$

where $k^2=\omega^2\mu\varepsilon$. Using (2.84) and relation (2.79), the total dyadic Green's functions of the cavity can be obtained. Assuming the current element is oriented in the y-direction, the electric-type dyadic component is obtained as

$$\begin{aligned} \mathbf{G}_{\mathrm{e}}^{\mathrm{yy}}\left(\mathbf{r},\mathbf{r}^{'}\right)=&\frac{1}{k^2}\sum_{n=0}^{\infty}\sum_{m=0}^{\infty}\sum_{l=0}^{\infty}\frac{\varepsilon_{0\mathrm{n}}\varepsilon_{0\mathrm{m}}\varepsilon_{0\mathrm{l}}\left[\left(\frac{l\pi}{c}\right)^2+\left(\frac{n\pi}{a}\right)^2\right]}{abc\left[k^2-\left(\frac{n\pi}{a}\right)^2-\left(\frac{m\pi}{b}\right)^2-\left(\frac{l\pi}{c}\right)^2\right]}\cdot \\ &\left(\sin\left(\frac{n\pi x}{a}\right)\sin\left(\frac{n\pi x^{'}}{a}\right)\cos\left(\frac{m\pi y}{b}\right)\cos\left(\frac{m\pi y^{'}}{b}\right)\sin\left(\frac{l\pi z}{c}\right)\sin\left(\frac{l\pi z^{'}}{c}\right)\right)-\frac{1}{k^2}\delta\left(r-r^{'}\right) \end{aligned} \tag{2.87}$$

In (2.87), the yy-component of the electric-type dyadic Green's function and consequently field distributions in the cavity are expanded versus the cavity modes in a simple closed-form relation. The cavity modes satisfy the following eigenvalue equation

$$\begin{aligned}\mathcal{L}(E) &= \left(\frac{\partial^2}{\partial x^2}+\frac{\partial^2}{\partial y^2}+\frac{\partial^2}{\partial z^2}+\omega^2\mu\varepsilon\right)E(x,y,z)\\ &= \lambda(\omega)\cdot E(x,y,z)\end{aligned} \tag{2.88}$$

where

$$\lambda(\omega) = \left(\omega^2\mu\varepsilon - \left(\frac{n\pi}{a}\right)^2 - \left(\frac{m\pi}{b}\right)^2 - \left(\frac{l\pi}{c}\right)^2\right) \tag{2.89}$$

represents the eigenvalue of the equation (2.88) and $m, n, l = 0, 1, 2, \ldots$. By sorting the eigenvalues with index n and representing the eigenmodes of the operator $\mathcal{L}$ in (2.88) by $\mathbf{J}_n(\mathbf{r};s)$, the Green's function in (2.88) in source-free regions can be written by

$$\overleftrightarrow{\mathbf{G}}_e\left(\mathbf{r},\mathbf{r}';s\right) = \sum_n \frac{1}{\lambda_n(s)} A_n \mathbf{J}_n(\mathbf{r};s)\mathbf{J}_n\left(\mathbf{r}';s\right) \tag{2.90}$$

According to (2.89) and (2.90), the singularity poles of the structure, which are the resonant frequencies of the cavity, are the zeroes of the eigenvalues in (2.89). It will be shown that the scattered field presented in (2.90) can be generalized for any arbitrary scattering scenario.

Returning to scattering from the chipless tag shown in Fig. 2.2, the incident electric field induces a current distribution on the tag, which can be calculated by applying boundary conditions on the tag surface as

$$\left\langle \overleftrightarrow{\mathbf{G}}\left(\mathbf{r},\mathbf{r}';s\right), \mathbf{J}\left(\mathbf{r}'\right)\right\rangle_{\mathbf{r}'} = -\mathbf{E}_t^{inc}(\mathbf{r};s) \qquad \forall \mathbf{r}\in A \tag{2.91}$$

Where $\hat{\mathbf{G}}$ in the following formulations is the electric-type dyadic Green's function and A represents the surface of the tag. The eigenvalue equation associated with (2.91) is written by

$$\left\langle \overleftrightarrow{\mathbf{G}}\left(\mathbf{r},\mathbf{r}';s\right), \mathbf{J}_n\left(\mathbf{r}';s\right)\right\rangle_{\mathbf{r}'} = \lambda_n(s)\mathbf{J}_n(\mathbf{r};s) \qquad \forall \mathbf{r}\in A \tag{2.92}$$

where $\mathbf{J}_n(\mathbf{r};\, s)$ and $\lambda_n(s)$ are nth eigenmode and eigenvalue of $\overleftrightarrow{\mathbf{G}}$, respectively. By applying the method of moment (MoM), the integral equation in (2.91) is converted to the following matrix equation

$$\mathbf{\Gamma}(s)\cdot\mathbf{J}(s) = \mathbf{I}_e(s) \tag{2.93}$$

and the eigenvalue equation corresponding to (2.93) is written by

$$\boldsymbol{\Gamma}(s) \cdot \mathbf{J}_{\mathrm{n}}(s) = \lambda_{\mathrm{n}}(s)\mathbf{J}_{\mathrm{n}}(s) \tag{2.94}$$

In order to have nontrivial solutions, the determinant of the coefficient matrix must be zero as

$$C = \det(\boldsymbol{\Gamma}(s) - \lambda_{\mathrm{n}}(s)\mathbf{I}) = 0 \tag{2.95}$$

C, is called the characteristic equation and $\mathbf{I}$, is a unit matrix. Assuming $\boldsymbol{\Gamma}$ to be a square matrix of rank N, one can write

$$\det(\boldsymbol{\Gamma}(s)) = \prod_{n=1}^{N} \lambda_{\mathrm{n}}(s) \tag{2.96}$$

The eigenvalues may or may not all be distinct. It is clearly seen from (2.95) and (2.96) that the CNRs of the scatterer are the zeroes of the eigenvalues. Each eigenvalue may contain an infinite number of CNRs. For each square matrix, two sets of eigenmodes, right-side and left-side, are defined. In (2.94), the right-side eigenmodes are introduced, which are represented by $\mathbf{J}_{\mathrm{n}}^{\mathrm{R}}$ in the following. The left-side Eigenmodes are defined as [45]

$$\mathbf{J}_{\mathrm{n}}^{\mathrm{L}}(s) \cdot \boldsymbol{\Gamma}(s) = \lambda_{\mathrm{n}}(s)\mathbf{J}_{\mathrm{n}}^{\mathrm{L}}(s) \tag{2.97}$$

The orthogonality and bi-orthogonality relations between eigenmodes can be summarized as [45]

$$\mathbf{J}_{\mathrm{n}}^{\mathrm{L}}(s) \cdot \mathbf{J}_{\mathrm{m}}^{\mathrm{L}}(s) = \delta_{\mathrm{mn}} \tag{2.98a}$$

$$\mathbf{J}_{\mathrm{n}}^{\mathrm{R}}(s) \cdot \mathbf{J}_{\mathrm{m}}^{\mathrm{R}}(s) = \delta_{\mathrm{mn}} \tag{2.98b}$$

$$\mathbf{J}_{\mathrm{n}}^{\mathrm{L}}(s) \cdot \mathbf{J}_{\mathrm{m}}^{\mathrm{R}}(s) = \delta_{\mathrm{mn}} \tag{2.98c}$$

where

$$\delta_{\mathrm{mn}} = \begin{cases} 0 & m \neq n \\ 1 & m = n \end{cases}$$

The current distribution and incident electric field in (2.94) can be expanded versus the eigenmodes as

$$\mathbf{J}(s) = \sum_{n=1} a_{\mathrm{n}} \mathbf{J}_{\mathrm{n}}^{\mathrm{R}}(s) \tag{2.99}$$

$$\mathbf{I}_{\mathrm{e}} = \sum_{n=1} b_{\mathrm{n}} \mathbf{J}_{\mathrm{n}}^{\mathrm{R}}(s) \tag{2.100}$$

Substituting (2.99) into (2.93) and using (2.97), one arrives at

$$\sum_{n=1} a_n \boldsymbol{\Gamma}(s) \cdot \mathbf{J}_n^{(R)}(s) = \sum_{n=1} a_n \lambda_n(s) \mathbf{J}_n^{(R)}(s) = \mathbf{I}_e(s) \tag{2.101}$$

By taking an inner product of the two sides of (2.101) with $\mathbf{J}_n^{(L)}(s)$ and using the orthogonality relation in (2.98a, 2.98b and 2.98c), one can write

$$a_n = \frac{1}{\lambda_n(s)} \cdot \frac{\mathbf{J}_n^{(L)}(s) \cdot \mathbf{I}(s)}{\mathbf{J}_n^{(L)}(s) \cdot \mathbf{J}_n^{(R)}(s)} \tag{2.102}$$

Therefore, the current distribution on the tag is written by

$$\mathbf{J}(s) = \sum_{n=1} \frac{1}{\lambda_n(s)} \cdot \frac{\mathbf{J}_n^{(L)}(s) \cdot \mathbf{I}(s)}{\mathbf{J}_n^{(L)}(s) \cdot \mathbf{J}_n^{(R)}(s)} \mathbf{J}_n^{(R)}(s) \tag{2.103}$$

By defining the normalized dyadic functions as

$$\mathbf{d}_n(s) = \frac{\mathbf{J}_n^{(R)}(s) \mathbf{J}_n^{(L)}(s)}{\mathbf{J}_n^{(R)}(s) \cdot \mathbf{J}_n^{(L)}} \tag{2.104}$$

the current distribution in (2.103) can be expressed by

$$\mathbf{J}(s) = \sum_n \frac{1}{\lambda_n(s)} \mathbf{d}_n(s) \cdot \mathbf{I}(s) \tag{2.105}$$

By comparing (2.93) and (2.105), one can write

$$\boldsymbol{\Gamma}^{-1} = \sum_n \frac{1}{\lambda_n(s)} \mathbf{d}_n(s) \tag{2.106}$$

It shows that the singularity poles of the scatterer are the zeroes of the Eigenvalues. Similarly,

$$\boldsymbol{\Gamma} = \sum_n \lambda_n(s) \mathbf{d}_n(s) \tag{2.107}$$

Therefore,

$$(\boldsymbol{\Gamma}(s))^{-1} \cdot \boldsymbol{\Gamma}(s) = \sum_n \mathbf{d}_n = \boldsymbol{\delta} \tag{2.108}$$

In some scattering problems, the geometry of the scatterer is perfectly matched to a specific coordinate system. As an example, when the incident electric field

illuminates a perfectly electric conducting (PEC) sphere or an infinite cylinder, the scattered fields or equivalently the induced currents on the scatterer can be easily expanded versus the eigenmodes of the structures [45, 46]. For arbitrary geometries, which are not necessarily compatible with any specific coordinate system, the numerical evolution of the eigenmode equation (2.97) can be used in order to find the eigenmodes, eigenvalues and, consequently, the complex natural resonances of the scatterer.

2.4 Theory of Characteristic Modes

In the previous section, the current and consequently, the radiated fields from the scatterer were expanded versus the eigenmodes of the dyadic Green's function of the structure in the complex frequency domain. The resulted matrix from MoM is not Hermitian and its eigenmodes and eigenvalues are complex. For well-coordinated structures such as sphere, the eigenmodes of the dyadic Green's function are in-phase on the surface of the scatterer in the spherical coordinate system. By changing the geometry of the scatterer, the eigen-currents will not be in-phase anymore. The question is how to extend the idea of in-phase basis functions for arbitrary-shape scatterer. The theory of characteristic modes introduces a weighted eigenvalue equation whose eigenvalues are in-phase on the scatterer surface. This theory was first introduced by Garbacz in 1971 for conducting bodies of arbitrary shapes [47]. His proposed approach was based on diagonalizing the scattering matrix of the scatterers. He presented a new class of eigenmodes on a scatterer that are real and their corresponding scattered fields have constant phase over the surface of the body. Although the proposed method was used in some cases, its implementation was not easy for an arbitrarily-shaped scatterer. In [48], Harrington proposed an alternative viewpoint for diagonalizing an operator. This technique relates the current distribution to the tangential electric field on the body. He defined a particular weighted eigenvalue equation, which gives the same eigenmodes defined by Garbacz, but with a simpler approach. Ever since, this proposed technique has been widely employed in the design and modeling of antennas and scatterers [49–52]. Similar to natural resonant modes, the characteristic modes are independent of source fields and depend only on the geometry and shape of a scatterer.

2.4.1 Mathematical Formulation of the Characteristic Mode Theory

Referring to Fig. 2.2, it is assumed that an incident plane wave illuminates the tag. The first step in formulating the eigenvalue equation, which defines the

characteristic modes of the tag, is the application of the electric-field integral equation (EFIE) on the tag surface as

$$\begin{aligned}\mathcal{L}(J) &= \left\langle \overleftrightarrow{\mathbf{G}}(\mathbf{r},\mathbf{r}';s),\mathbf{J}(\mathbf{r}') \right\rangle_{\mathbf{r}'} \\ &= -\mathbf{E}_{\mathrm{t}}^{\mathrm{inc}}(\mathbf{r};s)\end{aligned} \tag{2.109}$$

where $\overleftrightarrow{\mathbf{G}}$ is defined in (2.15) and the integration is performed over the surface of the tag. Since the operator $\mathcal{L}(.)$ in (2.109) has the dimensions of impedance, it is more convenient to introduce the notation

$$\mathcal{Z}(\mathbf{J}) \;=\; \mathcal{L}(\mathbf{J}) \tag{2.110}$$

where $\mathcal{Z}$ is a symmetric operator as

$$\langle B, \mathcal{Z}(C)\rangle = \langle \mathcal{Z}(B), C\rangle \tag{2.111}$$

One can write $\mathcal{Z}$ in terms of its real and imaginary components

$$\mathcal{Z} = \mathcal{R} + j\mathcal{X} \tag{2.112}$$

where

$$\mathcal{R} = \frac{1}{2}(\mathcal{Z} + \mathcal{Z}^*)$$
$$\mathcal{X} = \frac{1}{2j}(\mathcal{Z} - \mathcal{Z}^*)$$

Since the radiated power from a current distribution $\mathbf{J}$ on the tag is given by

$$P = \langle \mathbf{J}^*, \mathcal{R}(\mathbf{J})\rangle \tag{2.113}$$

it follows that $\mathcal{R}$ is positive semi-definite. The starting step in defining the characteristic modes of the tag is the following eigenvalue equation

$$\mathcal{Z}(\mathbf{J}_{\mathrm{n}}) = \gamma_{\mathrm{n}}\mathcal{M}(\mathbf{J}_{\mathrm{n}}) \tag{2.114}$$

where γ_{n} and $\mathbf{J}_{\mathrm{n}}$ are the nth eigenvalue and eigenmode of the equation and $\mathcal{M}$ is a weighting operator. Choosing $\mathcal{M} = \mathcal{R}$ ensures orthogonality of the radiation patterns of the current modes in the far zone. Introducing

$$\gamma_{\mathrm{n}} = 1 + j\lambda_{\mathrm{n}} \tag{2.115}$$

into (2.114) , the eigenvalue equation is converted to

$$\mathcal{X}(\mathbf{J}_n) = \lambda_n \mathcal{R}(\mathbf{J}_n) \tag{2.116}$$

Since $\mathcal{R}$ and $\mathcal{X}$ are real symmetric operators, both the eigenvalues λ_n and the corresponding characteristic modes, $\mathbf{J}_n$, must be real. In addition, the eigenmodes satisfy the orthogonality relationships

$$\langle \mathbf{J}_m, \mathcal{R}(\mathbf{J}_n) \rangle = \delta_{mn} \tag{2.117a}$$

$$\langle \mathbf{J}_m, \mathcal{X}(\mathbf{J}_n) \rangle = \lambda_n \delta_{mn} \tag{2.117b}$$

$$\langle \mathbf{J}_m, \mathcal{Z}(\mathbf{J}_n) \rangle = (1 + j\lambda_n)\delta_{mn} \tag{2.117c}$$

where

$$\delta_{mn} = \begin{cases} 1 & m = n \\ 0 & m \neq n \end{cases}$$

2.4.2 Characteristic Fields

The electric and magnetic fields produced by an eigenmode $\mathbf{J}_n$ on the surface of the tag are called characteristic fields, and are referred to as ($\mathbf{E}_n$, $\mathbf{H}_n$). One important property of the eigenfields is their orthogonality in the far zone. Based on Poynting's Theorem, the mutual power coupling between the current modes $\mathbf{J}_n$ and $\mathbf{J}_m$ distributed on the surface of the tag can be written as follows

$$\begin{aligned} P_{mn} &= \langle \mathbf{J}_m{}^*, \mathcal{Z}(\mathbf{J}_n) \rangle \\ &= \langle \mathbf{J}_m{}^*, \mathcal{R}(\mathbf{J}_n) \rangle + j\langle \mathbf{J}_m{}^*, \mathcal{X}(\mathbf{J}_n) \rangle \\ &= \int_{S'} \mathbf{E}_m \times \mathbf{H}_n{}^* \cdot ds + j\omega \iiint_{v'} (\mu \mathbf{H}_m \cdot \mathbf{H}_n{}^* - \varepsilon \mathbf{H}_m \cdot \mathbf{H}_n{}^*) dv \end{aligned} \tag{2.118}$$

Here, S' is any surface enclosing the tag and v' is the region enclosed by S'. According to the orthogonality relations in (2.117a, 2.117b, and 2.117c), we have

$$P_{mn} = (1 + j\lambda_n)\delta_{mn} \tag{2.119}$$

If S' is chosen to be a sphere at infinity, then the Eigenfields in the far zone can be expressed by

$$\begin{aligned} \mathbf{E}_n &= -\eta \hat{r} \times \mathbf{H}_n \\ &= \frac{-j\omega\mu}{4\pi r} e^{-jkr} \mathbf{F}_n(\theta, \phi) \end{aligned} \tag{2.120}$$

where $\eta = \sqrt{\mu/\varepsilon}$ is the intrinsic impedance of space, $\hat{r}$ is the unit radial vector perpendicular to S', (θ, φ) are the angular coordinates of the position on S' and $\mathbf{F}_n$ is the pattern of the field. Inserting the far-zone fields in (2.118), the real and imaginary parts of the radiated power can easily be separated as

$$\int_{S'} \mathbf{E}_m \times \mathbf{H}_n{}^* \cdot d\mathbf{s} = \delta_{mn} \tag{2.121}$$

$$\omega \iiint_{v'} (\mu \mathbf{H}_m \cdot \mathbf{H}_n{}^* - \varepsilon \mathbf{E}_m \cdot \mathbf{E}_n{}^*) dv = \lambda_n \delta_{mn} \tag{2.122}$$

Relation (2.121) expresses the orthogonality of the eigenfields in the far-zone region. For a single characteristic mode, (2.122) is written by

$$\omega \iiint_{v'} (\mu \mathbf{H}_n \cdot \mathbf{H}_n{}^* - \varepsilon \mathbf{E}_n \cdot \mathbf{E}_n{}^*) dv = \lambda_n \tag{2.123}$$

From (2.123), it is seen that at resonant frequencies where the electric and magnetic energies are equal, the corresponding eigenvalues are zero. At frequencies where $\lambda_n > 0$, the fields are inductive and for $\lambda_n < 0$, the fields are capacitive. According to (2.116), at resonant frequencies, we have

$$\mathrm{X}(\mathbf{J}_n) = 0 \tag{2.124}$$

By applying MoM and converting equation (2.124) into matrix equation, the determinant of the reactance matrix should be zero at the resonant frequencies of the structure in order to have nontrivial solutions.

2.4.3 Modal Solution

The current distribution on the tag can be expanded in terms of the characteristic current modes as

$$\mathbf{J} = \sum_{n=1} a_n \mathbf{J}_n \tag{2.125}$$

where $\mathbf{J}_n$ is the nth characteristic mode and a_n is the unknown coefficient in the expansion series. Substituting (2.125) in (2.109) and considering the linearity of the operator, we have

$$\sum_n a_n \mathcal{Z}(\mathbf{J}_n) = -\mathbf{E}_t^{\mathrm{inc}} \tag{2.126}$$

By taking an inner product of the two sides of (2.126) with $\mathbf{J}_m$ and using the orthogonality relations in (2.117a, 2.117b, and 2.117c), one can write

$$a_n = -\frac{\langle \mathbf{E}_t^{\mathrm{inc}}, \mathbf{J}_n \rangle}{\langle \mathbf{J}_n, \mathcal{Z}(\mathbf{J}_n) \rangle} = -\frac{\langle \mathbf{E}_t^{\mathrm{inc}}, \mathbf{J}_n \rangle}{1 + j\lambda_n} \tag{2.127}$$

It is seen that the unknown coefficients are strongly dependent on the coupling between the characteristic modes and the incident electric field. By substituting (2.127) in (2.125), the current distribution on the tag is given by

$$\mathbf{J} = -\sum_{n=1} \frac{\left\langle \mathbf{E}_{\mathrm{t}}^{\mathrm{inc}}, \mathbf{J}_{\mathrm{n}} \right\rangle}{1 + j\lambda_n} \mathbf{J}_{\mathrm{n}} \quad = -\sum_{n=1} \frac{V_{\mathrm{n}}}{1 + j\lambda_{\mathrm{n}}} \mathbf{J}_{\mathrm{n}} \tag{2.128}$$

where

$$V_{\mathrm{n}} = \left\langle \mathbf{E}_{\mathrm{t}}^{\mathrm{inc}}, \mathbf{J}_{\mathrm{n}} \right\rangle \tag{2.129}$$

is the coupling coefficient between nth characteristic mode and incident electric field. The electric and magnetic fields scattered from the tag can be written by

$$\mathbf{E} = -\sum_{n=1} \frac{V_{\mathrm{n}}}{1 + j\lambda_{\mathrm{n}}} \mathbf{E}_{\mathrm{n}} \tag{2.130}$$

$$\mathbf{H} = -\sum_{n=1} \frac{V_{\mathrm{n}}}{1 + j\lambda_{\mathrm{n}}} \mathbf{H}_{\mathrm{n}} \tag{2.131}$$

2.4.4 *Modal Significance and Characteristic Angle*

The variation of eigenvalues, current distribution, and corresponding eigenfields versus frequency provides some useful information about the scattering properties of the tag structure. The modal expansion of the current in (2.128) is inversely dependent on the eigenvalues as

$$MS_{\mathrm{n}} = \left| \frac{1}{1 + j\lambda_{\mathrm{n}}} \right| \tag{2.132}$$

This parameter is called the modal significance. This parameter depends only upon the geometry and dimensions of the tag, and does not vary with the incident excitation. Another parameter, which is very useful in calculating the quality factor of the scatterer at resonant frequencies, is the characteristic angle defined as

$$\alpha_{\mathrm{n}} = 180^{\circ} - \tan^{-1}(\lambda_{\mathrm{n}}) \tag{2.133}$$

This parameter models the phase angle between a characteristic current, $\mathbf{J}_{\mathrm{n}}$, and the associated characteristic field, $\mathbf{E}_{\mathrm{n}}$. It is clear from (2.132) and (2.133) that at the resonant frequencies of the tag, the characteristic angle is equal to zero and the modal significance has a maximum value of one. These parameters are very useful in calculating the quality factor of the tag at resonant frequencies. As an example, Fig. 2.22 shows the variation of the first two eigenvalues and modal significances

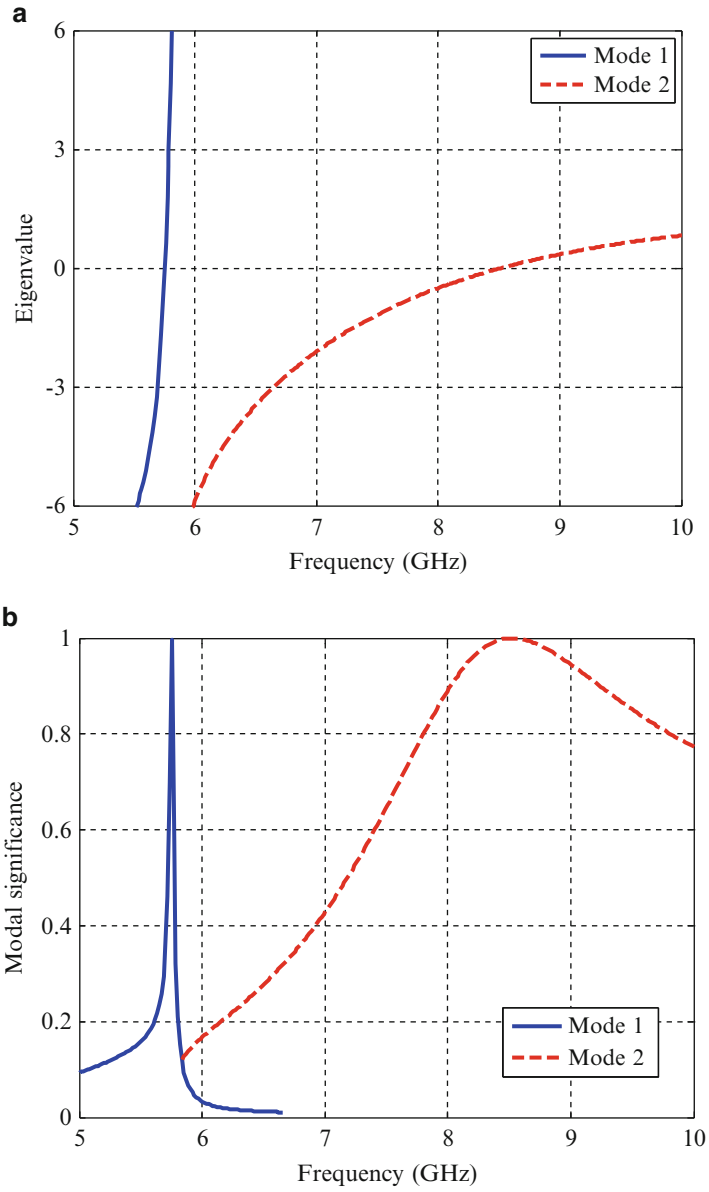

Fig. 2.22 (**a**) Eigenvalues and (**b**) modal significance of the first two characteristic modes of a chipless RFID tag versus frequency

versus frequency for a typical scatterer. In computing the radiating bandwidth of the modes, we need to know the frequencies at which the radiated power is half of that at resonant frequencies. From (2.132), at the frequencies where $\lambda_n = 1$ or $\lambda_n = -1$, the corresponding modal significance is 0.707, and the corresponding characteristic

angles are 135° and 225°. Labelling these frequencies f_L and f_H, the quality factor of the characteristic mode at resonant frequency can be calculated from the expression

$$Q \approx \frac{f_0}{f_H - f_L} \tag{2.134}$$

This approximation is only valid for high-Q resonators. There have been numerous formulae for calculating the quality factor of a scatterer. In our application where we try to implement resonators with high quality factor, all the proposed formulae give approximately the same results with slight variations. Another simple formula useful in calculating the quality factor of the resonators embedded on chipless RFID tags is given by the expression

$$Q_n = \frac{\omega}{2}\frac{d\lambda_n}{d\omega} \tag{2.135}$$

which was proposed by Harrington [53].

References

1. Baum CE (2012) The singularity expansion method in electromagnetics: a summary survey and open questions. SUMMA Foundation, Akron, OH
2. Baum CE (1971) On the singularity expansion method for the solution of electromagnetic interaction problems. Interaction Note 88, Air Force Weapons Lab., pp 1–111
3. Tesche F (1973) The far-field response of a step-excited linear antenna using SEM. IEEE Trans Antenna Propag 23(6):834–838
4. Baum CE (1986) The singularity expansion method: background and developments. IEEE Antennas Propag Soc Newslett 28(4):14–22
5. Barnes PR (1972) On the singularity expansion method as applied to the EMP analysis and simulation of the cylindrical dipole antenna. AFWL Interaction Note 146, Apr 1972
6. Umashankar KR, Wilton DR (1972) Transient scattering by a thin wire in free space and above ground plane using the singularity expansion method. AFWL Interaction Note 236, Apr 1972
7. Umashankar KR, Wilton DR (1974) Transient scattering characterization of circular loop using singularity expansion method. AFWL Interaction Note 259, 1974
8. Martinez JP, Pine ZL, Tesche FM (1972) Numerical results of the singularity expansion method as applied to a plane wave incident on a perfectly conducting sphere. AFWL Interaction Note 112, 1972
9. Dolph CL, Cho SK (1980) On the relationship between the singularity expansion method and the mathematical theory of scattering. IEEE Trans Antennas Propag 28(6):888–897
10. Baum CB (1976) Emerging technology for transient and broad-band analysis and synthesis of antennas and scatterers. Proc IEEE 64(11):1598–1616
11. Licul S, Davis WD (2005) Unified frequency and time-domain antenna modeling and characterization. IEEE Trans Antennas Propag 53(9):2882–2888
12. Licul S, Davis WD (2004) Pole/residue modeling of UWB antenna systems. IEEE antennas and propagation society international symposium, 2004, pp 1748–1751
13. Davis WA, Licul S (2004) Ultra-wideband antennas, in Introduction to Ultra-Wideband Communications. Reed JH (eds) Englewood Cliffs, NJ: Prentice-Hall

14. Caratelli D, Yarokoy A (2010) Unified time- and frequency-domain approach for accurate modeling of electromagnetic radiation processes in ultrawideband antennas. IEEE Trans Antennas Propag 58(10):3239–3255
15. Bedrosian G (1977) Stick-model characterization of natural frequencies and natural modes of the aircraft. AFWL Interaction Note 326, 1977
16. Rothwell EJ, Nyquist DP, Chen YF, Drachman B (1985) Radar target discrimination using the excitation-pulse technique. IEEE Trans Antennas Propag 33(9):929–937
17. Li Q, Ilavarasan P, Ross JE, Rothwell EJ (1998) Radar target identification using a combined early-time/late-time E-pulse technique. IEEE Trans Antennas Propag 46(9):1272–1278
18. Chen YF, Nyquist DP, Rothwell EJ, Webb L, Drachman B (1986) Radar target discrimination by convolution of radar return with extinction-pulses and single-mode extraction signals. IEEE Trans Antennas Propag 34(7):896–904
19. Baum CE (1996) Discrimination of buried targets via the singularity expansion. AFWL Interaction Note 521, 1996
20. Chen CC, Peters L Jr, Burnside WD (1995) Ground penetration radar target classification via complex natural resonances. Antennas and Propagation Society International Symposium, pp 1586–1589
21. Chen CC, Higgins MB, O'Neill K, Detsch R (1997) Buried unexploded ordnance identification via complex natural resonances. IEEE Trans Antennas Propag 45(11):1645–1654
22. Blischak A, Manteghi M (2009) Pole residue techniques for chipless RFID detection. In Antennas and Propagation Society International Symposium, 2009. APSURSI '09. IEEE, pp 1–4.
23. Blischak AT, Manteghi M (2011) Embedded singularity chipless RFID tags. IEEE Trans Antennas Propag 59:3961–3968
24. Rezaiesarlak R, Manteghi M (2014) Complex-natural-resonance-based design of chipless RFID tag for high density data. IEEE Trans Antennas Propag 52:3109–3121
25. Hong SK, Davis WA (2013) Use of tumor-specific resonance for more efficient microwave hyperthermia of breast cancer. Microw Opt Technol Lett 55(11):2659–2665
26. Hong SK, Davis WA (2012) Use of tumor-specific resonances in microwave hyperthermia of breast. In Antennas and Propagation Society International Symposium (APSURSI), 2012 IEEE
27. Manteghi M, Cooper DB, Vlachos PP (2012) Application of singularity expansion method for monitoring the deployment of arterial stents. Microw Opt Technol Lett 54(10):2241–2246
28. Van Bladel J (2007) Electromagnetic fields, 2nd edn. IEEE Press, New York
29. Salehi M, Manteghi M (2014) Transient characteristics of small antennas. IEEE Trans Antennas Propag 65:2418–2429
30. Salehi M, Manteghi M (2013) A wideband frequency-shift keying modulation technique using transient state of a small antenna. Prog Electromagnet Res 143:421–445
31. Salehi M, Manteghi M (2014) Self-contained compact transmitter for high-rate transmission. Electron Lett 50(4):313–316
32. Schelkunoff SA (1944) Representation of impedance functions in terms of resonant frequencies. Proc IRE 32(2):83–90
33. Baum CE (1976) The singularity expansion method. In: Transient electromagnetic fields. Springer, New York
34. Jin J-M (2010) Theory and computation of electromagnetic fields. Wiley, Hoboken, NJ
35. Carrier G, Krook M, Pearson C (1966) Functions of a complex variable. McGraw Hill, New York
36. Baum CE, Pearson LW (1981) On the convergence and numerical sensitivity of the SEM pole-series in early-time scattering response. Electromagnetics 1(2):209–228
37. Heyman E, Felsen LB (1985) A wavefront interpretation of the singularity expansion method. IEEE Trans Antennas Propag 37(7):706–718
38. Felsen LB (1984) Progressive and oscillatory waves for hybrid synthesis of source excited propagation and diffraction. IEEE Trans Antennas Propag 32:775–796

39. Heyman E, Felsen LB (1982) Creeping waves and resonances in transient scattering by smooth convex objects. IEEE Trans Antennas Propag 31:426–437
40. Altes RA (1976) Sonar for generalized target description and its similarity to animal echolocation systems. J Acoust Soc Am 59:97–106
41. Li L, Tan AE, Jhamb K, Rambabu K (2013) Characteristics of ultra-wideband pulse scattered from metal planar objects. IEEE Trans Antennas Propag 61(6):3197–3206
42. Tesche FM (1973) On the analysis of scattering and antenna problems using the singularity expansion technique. IEEE Trans Antennas Propag 21(1):53–62
43. Chen-To Chai (1994) Dyadic green function in electromagnetic theory. IEEE press series on electromagnetic waves. IEEE Press, New York
44. Rahmat-samii Y (1975) On the question of computation of the Dyadic Green's function at the source region in waveguides and cavities. Trans Microw Theory Tech 23(9):762–765
45. Baum CE (1975) On the Eigenmode expansion method for electromagnetic scattering and antenna problems, part 1: some basic relations for Eigenmode expansion, and their relation to the singularity expansion. Interaction Note 229, Air Force Weapons Lab., pp 1–94
46. Harrington RF (2001) Time-harmonic electromagnetic fields. Wiley-IEEE press, New York
47. Garbacz RJ, Turpin RH (1971) A generalized expansion for radiation and scattered fields. IEEE Trans Antennas Propag 19(1):348–358
48. Harrington RF, Mautz JR (1971) Theory of characteristic modes for conducting bodies. IEEE Trans Antennas Propag 19(5):622–628
49. Cabedo-Fabres M, Antonino-Daviu E, Valero-Nogueira A, Bataller MF (2007) The theory of characteristic modes revisited: a contribution to the design of antenna for modern applications. IEEE Antennas Propag Mag 49(5):52–68
50. Liu D, Garbacz PJ, Pozar DM (1990) Antenna synthesis and optimization using generalized characteristic modes. IEEE Trans Antennas Propag 38(6):862–868
51. Capek M, Hazdra P, Eicher J (2012) A method for the evaluation of radiation Q based on modal approach. IEEE Trans Antennas Propag 60(10):4556–4567
52. Rezaiesarlak R, Manteghi M (2014) On the application of characteristic modes for the design of chipless RFID tags. APS/URSI 2014, Memphis, TN
53. Harrington RF, Mautz JR (1972) Control of radar scattering by reactive loading. IEEE Trans Antennas Propag 20(4):446–454

Springer

http://www.springer.com/978-3-319-10168-2

Chipless RFID
Design Procedure and Detection Techniques
Rezaiesarlak, R.; Manteghi, M.
2015, VIII, 159 p. 148 illus., 80 illus. in color., Hardcover
ISBN: 978-3-319-10168-2